JGR Atmospheres

Key Points:
- Propagation of surface pressure anomalies explains the Lamb waveform derivative patterns seen in brightness temperature image differences
- 1-min mesoscale imagery depicts the short-period variations within the long-period wave packet envelope captured in full disk imagery
- The Lamb wave train appears dispersive, main pulse is followed by waves with decreasing wavelength of ∼40–80 km and period of ∼2.1–4.2 min

Correspondence to:
Á. Horváth,
hfakos@gmail.com

Author Contributions:
Conceptualization: Ákos Horváth
Formal analysis: Ákos Horváth
Funding acquisition: Ákos Horváth, Stefan A. Buehler
Investigation: Sharon L. Vadas, Claudia C. Stephan, Stefan A. Buehler
Methodology: Ákos Horváth, Sharon L. Vadas
Project Administration: Ákos Horváth, Stefan A. Buehler

One-Minute Resolution GOES-R Observations of Lamb and Gravity Waves Triggered by the Hunga Tonga-Hunga Ha'apai Eruptions on 15 January 2022

Ákos Horváth[1] , Sharon L. Vadas[2] , Claudia C. Stephan[3] , and Stefan A. Buehler[1]

[1]Meteorological Institute, Universität Hamburg, Hamburg, Germany, [2]Northwest Research Associates, Boulder, CO, USA, [3]Leibniz Institute of Atmospheric Physics, University of Rostock, Kühlungsborn, Germany

Abstract We use high temporal-resolution mesoscale imagery from the Geostationary Operational Environmental Satellite-R (GOES-R) series to track the Lamb and gravity waves generated by the 15 January 2022 Hunga Tonga-Hunga Ha'apai eruption. The 1-min cadence of these limited area (∼1,000×1,000 km²) brightness temperatures ensures an order of magnitude better temporal sampling than full-disk imagery available at 10-min or 15-min cadence. The wave patterns are visualized in brightness temperature image differences, which represent the time derivative of the full waveform with the level of temporal aliasing being determined by the imaging cadence. Consequently, the mesoscale data highlight short-period variations, while the full-disk data capture the long-period wave packet envelope. The full temperature anomaly waveform, however, can be reconstructed reasonably well from the mesoscale waveform derivatives. The reconstructed temperature anomaly waveform essentially traces the surface pressure anomaly waveform. The 1-min imagery reveals waves with ∼40–80 km wavelengths, which trail the primary Lamb pulse emitted at ∼04:29 UTC. Their estimated propagation speed is ∼315 ± 15 m s⁻¹, resulting in typical periods of 2.1–4.2 min. Weaker Lamb waves were also generated by the last major eruption at ∼08:40–08:45 UTC, which were, however, only identified in the near field but not in the far field. We also noted wind effects such as mean flow advection in the propagation of concentric gravity wave rings and observed gravity waves traveling near their theoretical maximum speed.

Plain Language Summary The record-setting eruption of the Hunga Tonga-Hunga Ha'apai volcano on 15 January 2022 was observed by geostationary satellites, which take an image of the full Earth disk every 10–15 min. Several smaller areas (∼1,000 km on a side) are, however, imaged every 1 min. The eruption generated various waves in the atmosphere, including acoustic waves traveling at the speed of sound and slower gravity waves. These atmospheric waves can be tracked by the subtle brightness temperature changes they cause in the images. We show that the 1-min images used in our study capture finer details of the wave patterns and allow a better estimation of wave properties than the relatively infrequent full disk images. The high temporal frequency imagery also allows to determine the eruption sequence more precisely and reveal how the background winds affect the propagation of the waves.

1. Introduction

On 15 January 2022, the Hunga Tonga-Hunga Ha'apai submarine volcano (20.54°S, 175.38°W, hereafter HTHH) experienced a climactic eruption which produced a plume with overshooting tops reaching record-setting altitudes of 55–57 km (Carr et al., 2022; Proud et al., 2022). The eruption generated worldwide tsunamis (Kubota et al., 2022; Purkis et al., 2023), lofted unprecedented amounts of water vapor directly into the stratosphere to heights of 30–40 km (Khaykin et al., 2022; Millán et al., 2022; Randel et al., 2023), and perturbed the global electric circuit via extreme lightning activity (Bór et al., 2023).

Global seismic and microbarometer observations revealed that the eruption emitted a wide spectrum of acoustic and gravity waves, including audible sound, infrasound, and internal gravity waves (Matoza et al., 2022; Vergoz et al., 2022), which also caused significant changes in the ionosphere and thermosphere (Harding et al., 2022; Vadas, Becker, et al., 2023). Most prominent among them was a large-amplitude Lamb wave, which circled the Earth several times (Amores et al., 2022; Heki, 2022; Otsuka, 2022; Wright et al., 2022).

The Lamb wave is a special acoustic wave that is hydrostatically balanced in the vertical direction and propagates in the horizontal direction only. The ideal Lamb wave is a mode of an isothermal and windless atmosphere, where it propagates non-dispersively and isotropically with a nominal sound speed of $\sim$312 m s^{-1} (Bretherton, 1969). A similar mode exists in the real atmosphere and travels as an edge wave guided by the surface with most of its energy concentrated in the troposphere (Garrett, 1969). Real Lamb waves do show dispersion and waveform distortion, whose magnitude depends mostly on the global winds and to a lesser degree on the vertical temperature structure and topography encountered along the travel path (Garrett, 1969; Sepúlveda et al., 2023). Under standard atmospheric conditions, the phase speed of Lamb waves can easily vary between 294 and 319 m s^{-1} (Garrett, 1969). Lamb waves propagate very efficiently because their attenuation distance largely exceeds the circumference of the Earth. They appear as a pseudo-mode bridging the gap between the acoustic and gravity modes and can exist at all periods ranging from a few minutes to about a day (Francis, 1973).

Several studies tracked the global propagation of the primary Lamb wave emitted by HTHH using infrared brightness temperatures from geostationary satellites (Amores et al., 2022; Matoza et al., 2022; Otsuka, 2022; Winn et al., 2023). All of these studies used full disk (FD) imagery available either at 10-min cadence from the Advanced Baseline Imager (ABI) aboard the Geostationary Operational Environmental Satellite-R series (GOES-R) and the Advanced Himawari Imager (AHI) aboard the Himawari-8 satellite or at 15-min cadence from the Spinning Enhanced Visible and Infrared Imager (SEVIRI) aboard the Meteosat Second Generation satellites. From such FD imagery, the horizontal phase speed, horizontal wavelength, and ground-based period of the Lamb wave were estimated as $c_H \approx$ 303–323 m s^{-1}, $\lambda_H \approx$ 400–500 km and $\tau_R \approx$ 20–30 min, respectively.

Studies analyzing surface pressure records or numerically simulating the atmospheric waves and the triggered meteotsunamis arrived at similar or even longer Lamb wavelengths and periods. The far-field envelope of the complex pressure wave packet can be roughly approximated by an *N*-wave or a positive triangular pulse of 400–900 km width and 20–50 min duration (Heinrich et al., 2023; Kubota et al., 2022; Matoza et al., 2022; Vergoz et al., 2022; Watada et al., 2023; Winn et al., 2023).

In this study, we take advantage of the GOES-R mesoscale scans, which offer a limited-area ($\sim$1,000 $\times$ 1,000 km^2) view of the HTHH Lamb and gravity waves, but at an order of magnitude better temporal resolution of 1 min. We show that the long-period wave cannot be directly extracted from brightness temperature imagery against a highly varying background. The commonly used visualization technique of differencing image sequences characterizes instead the waveform time derivatives and thus constitutes a high-pass filter. Temporal aliasing due to a reduced sampling frequency, on the other hand, represents a compensating factor. As a result of these opposing effects, the FD difference imagery captures the long-period envelope of the full wave packet. However, it misses important high-frequency variations within the waveform, which can only be obtained from the mesoscale imagery.

The paper is organized as follows. Section 2 introduces the ABI mesoscale data. Section 3 explains the emergence of the specific wave patterns that can be visualized in brightness temperature image differences. Section 4 analyzes the first two passages of the Lamb waves and provides further examples of gravity waves captured in the high-resolution data. A discussion and conclusions are given in Section 5.

2. ABI 1-Minute Mesoscale Imagery

2.1. Mesoscale Domains

To identify and track atmospheric waves generated by the HTHH eruption, we used infrared (IR) imagery from ABI aboard GOES-17 (GOES-West) and GOES-16 (GOES-East). The vertical near-side perspective views of the Earth disk from the geostationary vantage points of GOES-17 and GOES-16 are depicted in Figures 1a and 1b, respectively. GOES-17, stationed at 137.2°W, observes the Pacific including HTHH, as well as Central and North America. The coverage area of GOES-16, stationed at 75.2°W, is centered on the Americas, but also includes the Eastern Pacific and parts of the Atlantic. The current ABI imaging Mode 6 scans the full disk every 10 min, the Pacific US (PACUS, GOES-17) and Continental US (CONUS, GOES-16) sectors every 5 min, and two mesoscale domains (M1, M2) per satellite every minute.

All previous studies used the 10-min FD imagery for the global tracking of the main Lamb wave. The PACUS and CONUS scans offer an improved 5-min temporal resolution over a $\sim$5,000$\times$3,000 km^2 sector covering the latitudes of the US (15°N–50°N). In this study, however, we exploit the mesoscale scans, which provide the highest cadence of 1 min, albeit in a limited area.
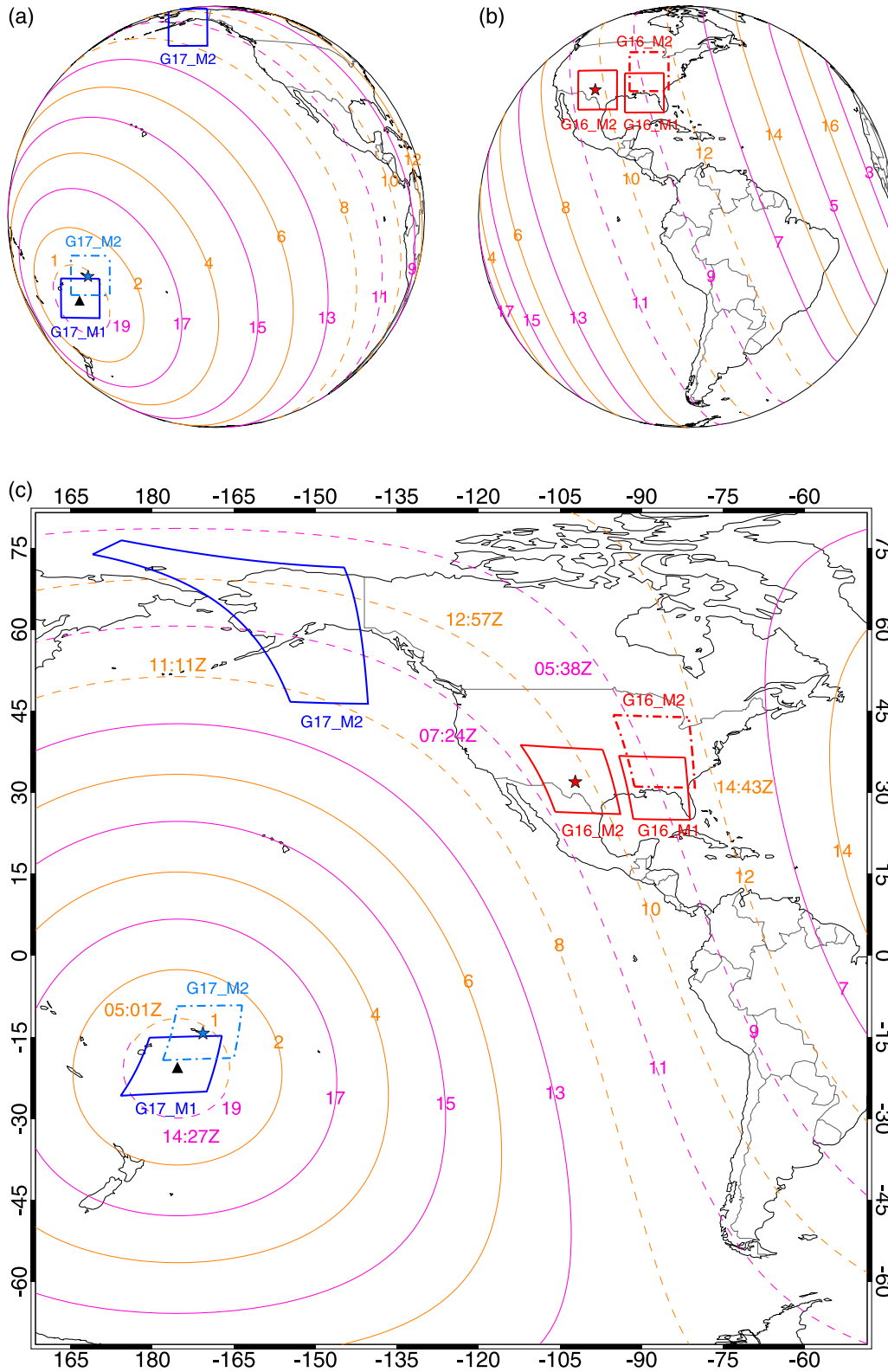
Figure 1.

A full disk IR image is given on a 5,424 × 5,424 fixed grid rectified to the Geodetic Reference System 1980 (GRS80) ellipsoid. The fixed grid has an angular sampling distance of 56 μrad, which corresponds to a spatial resolution of ~2 km at the subsatellite point. A mesoscale domain is a 500 × 500-pixel square subset of an FD image, covering a ~1,000 × 1,000 km^2 area at the subsatellite point. Each mesoscale domain can be independently retargeted from its default position to follow evolving features of interest, such as severe weather or volcanic eruptions.

The ABI mesoscale domains were moved several times during 15–16 January 2022. Figure 1 shows, in chronological order, only those locations that were used for tracking the waves triggered by the eruptions. The GOES-17 M2 domain was centered on American Samoa to the northeast of HTHH between 02:41 and 05:59 UTC on 15 January. The midpoint and southern edge of this domain were respectively 930 and 155 km from the volcano. Although this domain unfortunately missed the rising eruption column, it did however capture the earliest phases of wave propagation. In this domain, we used atmospheric surface pressure data collected in the National Park of American Samoa, Pago Pago (blue star in Figure 1) to explain the observed temperature anomaly waveform by the pressure anomaly waveform.

After a 1-hr gap, the GOES-17 M1 domain was centered on HTHH at 07:05 UTC on 15 January and kept there for a little over 2 days. This domain observed the spreading of the stratospheric and near-tropopause plumes produced by the main eruption at ~04:29 UTC and also captured the later smaller eruptions. These two domains provide a rich data source for the analysis of near-field wave phenomena.

The GOES-17 M2 domain was subsequently moved back to its default location over Alaska (~9,000 km from HTHH) and allowed the far-field observation of the A1 minor arc west-to-east wave passage between 11 and 14 UTC on 15 January. Additional far-field observations of the A1 wave passage over the southwest and southeast US were provided by the GOES-16 M2 domain (~9,500 km from HTHH) between 12 and 15 UTC and the GOES-16 M1 domain (~11,000 km from HTHH) between 15 and 17 UTC on 15 January. Surface pressure data at Midland International Air and Space Port (Midland, Texas; red star in Figure 1) located in the GOES-16 M1 domain was also analyzed.

The antipodal A2 major arc east-to-west wave passage on 16 January was first observed in the GOES-16 M2 domain, relocated to the southeastern US, and the GOES-16 M1 domain between 06 and 08 UTC. These two GOES-16 mesoscale domains cover nearly the same longitude range and half overlap with M2 being north of M1. The A2 wave passage was then imaged in the default GOES-17 M2 domain over Alaska between 08 and 11 UTC. Finally, the GOES-17 M1 domain captured the confluence and interference of the returning A2 waves over HTHH between 16:00–18:00 UTC.

Note that while the mesoscale scans are square images in the native fixed grid, they generally do not correspond to square areas in longitude-latitude space. As shown by the equirectangular projection in Figure 1c, the map distortion increases with increasing distance from the equatorial subsatellite point. As a result, the map distortion is largest for the default M2 domain over Alaska, which is near the limb of the GOES-17 full disk (in fact, its top left northwestern corner contains space pixels). There is significant east-west stretching at such oblique view angles, especially poleward of 60°N.

A related caveat is that although the fixed grid is a regular grid in the satellite coordinate system with an angular spacing of 56 μrad in both the east-west and north-south scan directions, it is an irregular grid in ellipsoid-projected distance. The nominal grid spacing (or ground resolution) is ~2 km only near the subsatellite point. Grid spacing generally increases with distance from the subsatellite point and shows significant variations within a given domain too. The horizontal distance between two neighboring image pixels is largest in the most obliquely-viewed GOES-17 M2 domain over Alaska, where it typically is in the range of 3–15 km. Grid spacing is finer in the rest of the domains, usually between 2.5 and 6.0 km. Therefore, when estimating the propagation

Figure 1. Geographic location of GOES-17 (G17, blue) and GOES-16 (G16, red) mesoscale domains (M1, M2) used for wave tracking on 15–16 January 2022: (a) GOES-17 fixed grid view, (b) GOES-16 fixed grid view, and (c) equirectangular projection. The black triangle is HTHH. The blue and red stars mark the location of surface air pressure measurements at the National Park of American Samoa and Midland International Air and Space Port, respectively. The orange and magenta lines indicate isodistances (×1,000 km) from the volcano and its antipode, respectively. Arrival times at the dashed isodistances (orange—15 January, magenta—16 January) are derived using a nominal propagation speed of 315 m s^{-1} and the emission time of the first detectable waves at 04:07 UTC on 15 January 2022. The temporal coverage of the mesoscale domains is summarized in Table S1 in Supporting Information S1.

speed of the observed waves, it is important to calculate ellipsoid-projected distances from the actual geodetic latitude and longitude of image pixels—we use the GRS80 ellipsoid.

2.2. Brightness Temperatures

Spectral radiances were converted to the equivalent black body brightness temperature, henceforth simply brightness temperature (*BT*), as described in the *GOES-R Series Product Definition and Users' Guide* (GOES-R, 2019). We track waves directly in the fixed grid square images (500×500 pixels) to avoid unnecessary remapping and interpolation. The waves are detectable in all IR channels to a varying degree. For illustrations in this paper, we use C7, C9, C11, C12, or C13, choosing the one that provides the sharpest signal for a given time and location.

For the interpretation of the observed wave patterns, it is important to have at least a qualitative understanding of the altitude ranges the brightness temperatures represent. Out of the 10 ABI IR channels, six are window channels (C7, C11, C13, C14, C15, C16) with a clear-sky vertical weighting (or contribution) function that peaks at the surface (Schmit et al., 2017). In these channels, a large portion of the signal originates from the surface in clear air, although water vapor, SO_2, and CO_2 also modulate the *BT* to various degrees. In the presence of opaque meteorological or volcanic clouds, however, the signal originates largely from the cloud altitude. In semitransparent clouds, there is still noticeable contribution from the surface and the *BT* is characteristic of an apparent height somewhere between the surface and cloud level.

The clear-sky weighting function of the lower-, mid-, and upper-level water vapor channels (C10, C9, C8) peak at ~4 km, ~6.5 km, and ~8.2 km altitude, respectively. Therefore, these channels are more representative of the mid to upper troposphere, although high-level clouds also affect the signal. Finally, the "ozone" channel (C12) has a clear-sky weighting function with a peak at the surface as well as at ~22 km altitude and, thus, characterizes the lower stratosphere (albeit water vapor absorbs in this channel too).

The vertical weighting functions are relatively broad and, hence, the clear-sky *BT* represents a weighted layer mean rather than a single level. Overall, the presence of a wave front in several IR channels and across different scene types is indicative of a vertically extensive and coherent wave.

We also note that the GOES-17 ABI suffered a loop heat pipe (LHP) anomaly, which prevents maintaining the IR detectors at their required temperatures during parts of the night under certain orbital conditions. After performance recovery steps, 97% of imaging capability in the thermal infrared bands was regained (McCorkel et al., 2019); however, image degradation such as increased noise and striping are occasionally noticeable.

3. Visualization of Atmospheric Waves

Differencing brightness temperature image sequences has been the main tool for the visualization of the atmospheric waves generated by the eruption. In this section, we investigate which part of the wave spectrum is in fact captured by such difference imagery.

3.1. The Surface Pressure Waveform

Atmospheric pressure anomalies caused by the HTHH eruption were recorded all around the globe. Laboratory measurements and numerical simulations show that acoustic waveforms propagating through the atmosphere can get strongly distorted mostly by thermal inhomogeneities and turbulent wind velocity fluctuations (Averiyanov et al., 2011; Stout, 2018; Yuldashev et al., 2017). Unlike the classic *N*-wave sonic boom, distorted waveforms can have rounded waves, several spikes, multiple shock fronts, and oscillations or even a maximum overpressure in the tail part. As a result, the observed HTHH Lamb wave packets are quite complex; nevertheless, their far-field envelopes can be roughly approximated by an *N*-wave or a positive triangular pulse (Matoza et al., 2022; Vergoz et al., 2022; Watada et al., 2023).

The amplitude of the pressure wave decreases with distance from the eruption, varying from ~30 hPa in Tonga (64 km from HTHH) to ~0.5 hPa in the far field (10k km from HTHH). The estimated duration (or "period") of the enveloping pulse is between 20 and 50 min, which corresponds to a horizontal width (or "wavelength") of 400–900 km for a phase velocity at the sound speed. The global propagation of this broad far-field atmospheric pressure pulse was well reproduced by Amores et al. (2022), who introduced an instantaneous sea level
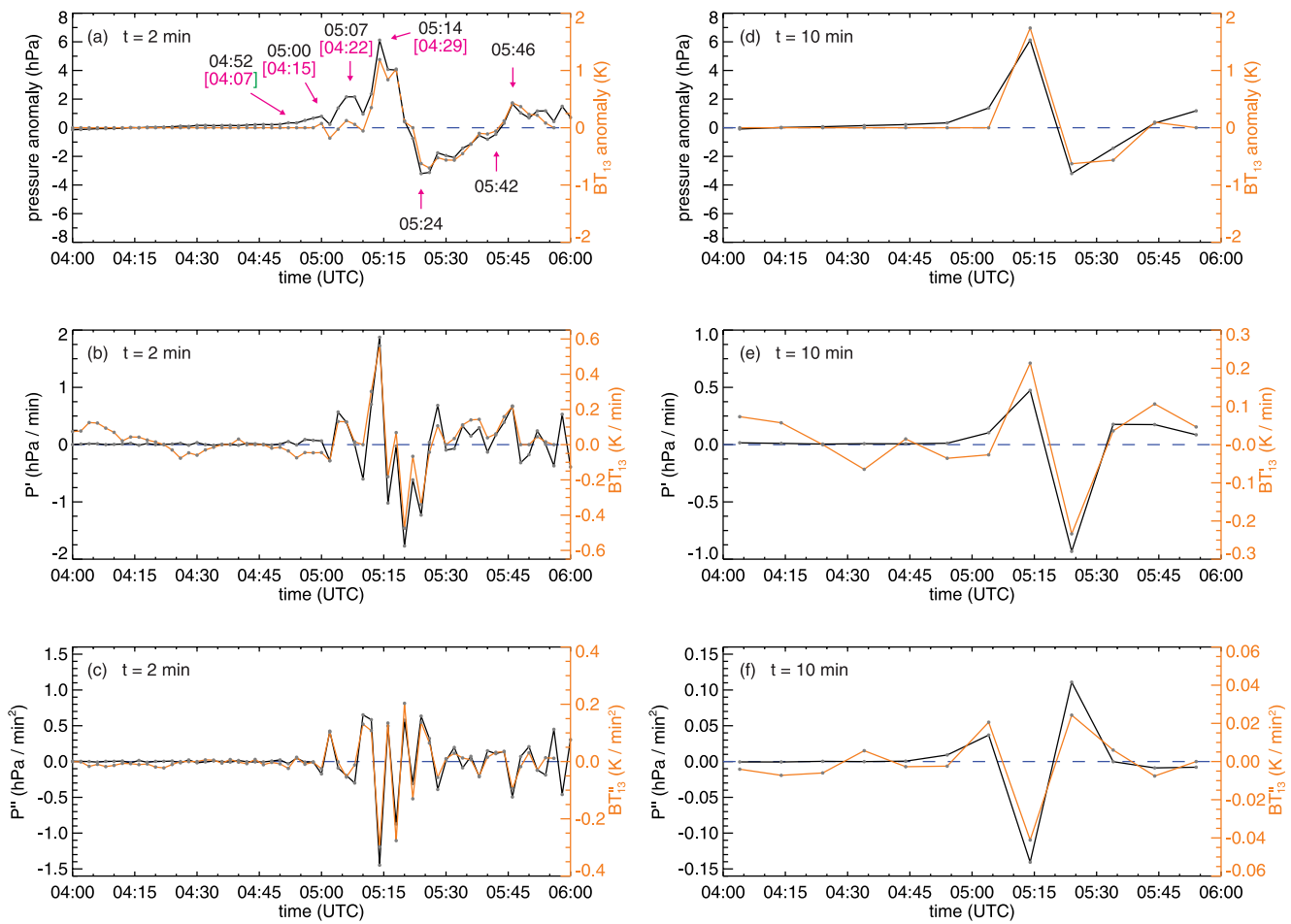
Figure 2. Atmospheric surface pressure (P, black) and channel 13 (10.3 μm) brightness temperature (BT_{13}, orange) waveforms and their time derivatives at $\Delta t = 2$ min sampling in Pago Pago, American Samoa between 04:00–06:00 UTC on 15 January 2022. (a) Pressure anomaly relative to the mean of the 04:00–04:30 period. The arrival times and the emission times (pink, in brackets) of individual pressure peaks are also indicated, assuming a propagation velocity of 315 m s^{-1}. The BT_{13} anomaly was reconstructed from the observed BT_{13}''. (b) The first time derivatives P' and BT_{13}'. (c) The second time derivatives P'' and BT_{13}''. The time derivatives of BT_{13} were averaged along the isodistance of Pago Pago to reduce noise. Panels (d), (e), and (f) are the same as (a), (b), and (c), respectively, but for $\Delta t = 10$ min.

perturbation in a shallow water ocean model as well as by Watanabe et al. (2022), who imposed an instantaneous hot anomaly over the volcano in an atmospheric general circulation model. The atmospheric Lamb wave triggered a meteotsunami, the accurate numerical simulation of which also required the imposition of such long-period and long-wavelength pressure pulses as forcing (Heinrich et al., 2023; Kubota et al., 2022; Suzuki et al., 2023; Winn et al., 2023; Yamada et al., 2022).

For acoustic waves such as the Lamb wave, the temperature perturbations are in phase with and proportional to the pressure perturbations (Vadas, 2013). Therefore, the waveform of surface pressure anomalies approximates, to first order, the waveform of the brightness temperature anomalies embedded in the satellite images. The black curve in Figure 2a shows the surface pressure anomaly measured at the National Park of American Samoa (Pago Pago, Tutuila Island) between 04:00–06:00 UTC on 15 January (PurpleAir, 2023). The barometer provides measurements at a temporal resolution of $\Delta t = 2$ min and is located ~850 km from HTHH near the center of our G17_M2 Samoa domain (14.27°S, 170.70°W; blue star in Figure 1). This distance translates to a wave travel time of ~45 min at the propagation speed of ~315 m s^{-1} derived in Section 4.1. The anomalies are given relative to the mean value of the 04:00–04:30 UTC period (1,006.5 hPa), when the pressure was very stable.

The first small pressure peak (~0.3 hPa) occurs at 04:52 UTC, corresponding to an emission time of ~04:07 UTC at HTHH. Although this pressure anomaly is barely discernible, it likely is a real signal, because its emission time agrees with that of the very first visually detectable wave in our mesoscale BT imagery. Seismo-acoustic

data (Matoza et al., 2022) and tsunami runup measurements in the Tonga Archipelago (Purkis et al., 2023) also indicate an explosive event at that emission time. In addition, Van Eaton et al. (2023) found a sudden increase in the plume's width at 04:07 UTC using GOES-17 full disk visible images.

This minor anomaly is followed by two larger anomalies at 05:00 UTC (~0.8 hPa, emission time 04:15 UTC) and 05:07 UTC (~2.1 hPa, emission time 04:22 UTC). The peak overpressure of ~6.1 hPa is recorded in Pago Pago at 05:14 UTC. The maximum HTHH plume-top height of 55–57 km was measured ~6 min after the 04:29 UTC emission time of this main pressure pulse (Carr et al., 2022). Matoza et al. (2022) also report seismo-acoustic events with ~04:15 UTC and ~04:30 UTC emission times, while Purkis et al. (2023) claim an explosive blast with a ~04:18 UTC emission time (in between the second and third peak in our pressure data).

The pressure quickly drops in the next 10 min, reaching its lowest value, a −3.2 hPa anomaly, at 05:24 UTC. Thus, the amplitude of the main explosion is ~9.3 hPa in Samoa. The pressure then recovers with some fluctuations by 05:42 UTC and shows a smaller trailing peak (~1.7 hPa) at 05:46 UTC.

The full wave packet is a combination of four consecutive explosions of increasing magnitude. A range of characteristic time spans can be derived, depending on whether one focuses on the main blast or the full packet. Extrapolating backward and forward in time from the primary pressure peak and trough, the main blast can be approximated by an *N*-wave starting at ~05:08 UTC and ending at ~05:32 UTC. This *N*-wave has a rise time of 6–8 min and a total duration of ~24 min. The time difference between the primary peak and the first trailing peak yields a slightly longer period of ~32 min. The duration of the full wave packet is ~50 min (04:52–05:42 UTC), comprising a ~28-min positive phase and a ~22-min negative phase. This range of time span estimates agrees with that reported in previous studies.

Figure S1 in Supporting Information S1 plots 1-min barometer readings (Joe LaPlante, personal communication) collected at nearby Coconut Point (Nu'uuli, Tutuila Island), which show essentially the same pressure waveform comprising of the main pulse and at least two preceding smaller pulses. Although this data has better temporal resolution, its quantization ($\Delta p = 0.34$ hPa) is significantly coarser than that of the 2-min pressure measurements ($\Delta p = 0.01$ hPa); hence, we use the latter to calculate waveform derivatives in the next section. Figure S1 in Supporting Information S1 also plots 1-min surface pressures at Midland International Air and Space Port (close to the center of the G16_M2 Texas domain; red star in Figure 1) obtained from the Automated Surface Observing System (ASOS, 2023). This far-field waveform (~9,716 km or ~8.5 hr from HTHH) is very similar to the near-field ones in Samoa, demonstrating the stability of the shock wave as it traversed the globe, but its amplitude is an order of magnitude smaller, ~0.9 hPa.

The black curve in Figure 2d demonstrates how the observed waveform changes when the $\Delta t = 10$ min cadence of full disk imagery is used. Here the 2-min pressure time series is subsampled backward and forward in time from 05:14 UTC to preserve the main peak. The smaller blasts and other fine details are indistinguishable and all that remains is the ~50-min envelope of the full wave packet. As chance would have it, the rise time and the time span of the peak-to-trough drop of the central *N*-wave are both close to 10 min; hence, the primary Lamb pulse is well represented even at the reduced FD sampling.

3.2. Waveform Time Derivatives

Visualizing the HTHH-induced temperature perturbations in raw *BT* imagery is rather problematic. The amplitude of the temperature variations rapidly decreases with distance and at most represents a signal of a couple of percent. Pressure perturbations have a similar relative magnitude, but they are superimposed on a fairly homogeneous and steady background. The temperature perturbations, in contrast, are superimposed on a heterogeneous and rapidly varying background. Spatiotemporal variations in clouds (advection, growth, dissipation) and to a lesser degree in water vapor and trace gases lead to a challenging background scene for the identification and tracking of faint wavelike features. The large dynamic range of *BT* makes it difficult to achieve enough local contrast both in cold (bright, cloudy) and warm (dark, clear sky) areas when tone mapping the image.

Waves are easier to detect in the time derivatives of the brightness temperature. For each pixel, we approximate the first time derivative of *BT* at time t using a backward finite-difference scheme

$$BT' = \frac{BT(t) - BT(t - \Delta t)}{\Delta t} \tag{1}$$

and the second time derivative using a second-order central finite-difference scheme

$$BT'' = \frac{BT(t + \Delta t) - 2BT(t) + BT(t - \Delta t)}{\Delta t^2}, \qquad (2)$$

where Δt is the time difference between the images. Apart from a scaling factor, the first time derivative is just the difference between two subsequent images, while the second time derivative is the difference between the mean of three subsequent images and the central image of the triplet.

The mesoscale images are available at a time resolution of $\Delta t = 1$ min. However, with a subsampling rate of $n > 1$, that is, selecting only every n th image from the sequence, we can investigate the spatiotemporal aliasing effect of longer sampling periods on the appearance of wave patterns. For example, a sampling period of $\Delta t = 10$ min mimics the GOES-R and Himawari-8 full-disk images that were used in previous studies.

It is important to note that these (discrete) time derivatives act as high pass filters, where higher frequencies get larger weights than lower frequencies. Before considering BT images, we first demonstrate the effect of the time differentiators on the pressure waveform, which is a proxy for the temperature waveform. The black curves in Figures 2b and 2c plot the first derivative (P') and second derivative (P'') of the Samoa pressure time series ($\Delta t = 2$ min), respectively. These can be thought of as the pressure (or BT) waveform derivatives at the image pixel which corresponds to the barometer's location. As shown, the differentiators emphasize the shorter period variations within the waveform rather than the long-period envelope of the full wave packet. The first time derivative is the pressure tendency, which characterizes the local steepness of the waveform. The second derivative describes the local concavity of the graph: the waveform is concave up (or convex) if $P'' > 0$ and concave down if $P'' < 0$.

The derivative of the waveform is frequently used in laboratory investigations of N-waves, especially ones with multiple shocks similar to the HTHH pressure wave. For example, the peak overpressure and the rise time are difficult to evaluate in distorted waveforms found in turbulent flow. These important acoustic wave parameters can be better defined based on the first derivative of the pressure waveform (Averiyanov et al., 2011; Yuldashev et al., 2017). Analyzing P' allows ranking shocks by strength (steepness), separating close shocks that otherwise might be considered as one long shock, and enables detecting shocks in the tail part of the packet.

The first and second derivatives of the pressure waveform sampled at the reduced FD rate of $\Delta t = 10$ min are given by the black curves in Figures 2e and 2f, respectively. In both cases, the maxima of the derivatives are separated by 20 min. By chance, this time span agrees well with the ~24 min duration of the N-wave that can be fitted to the primary Lamb pulse of the full wave packet.

3.3. Image Processing

3.3.1. Gray Scaling, Smoothing, Contrast Enhancement

Although it high pass filters the data, the major advantage of taking the time derivatives of BT is that it largely eliminates the high dynamic-range background image comprising a mixture of clear (warm) and cloudy (cold) areas. In the significantly reduced dynamic range BT derivatives, it is easier to achieve good local contrast throughout the entire scene. The time derivatives are first scaled to 256 gray levels using an appropriate initial range, for example, ± 1 K min^{-1} for BT' and ± 0.25 K min^{-2} for BT''. The images are then histogram equalized. Because this means a palette change for each image, we omit the colorbar in the figures and animations. For the visualization of wave fronts, however, spatial coherence is more important than pixel intensity (the magnitude of the time derivative). Histogram equalization readjusts the intensities and allows areas of lower local contrast to gain a higher contrast. In the resulting images, the bright wave crests and dark troughs respectively correspond to the maxima and minima of the waveform derivatives plotted in Figure 2.

The images are also smoothed with a moving average boxcar filter. The smallest averaging window of 3×3 pixels is already adequate, but in this study, we opt for a slightly larger 5×5-pixel window, which in our experience leads to a clearer separation of wave fronts. Mean filtering is applied in all cases, except in the analysis of the shortest wavelength (~15 km) gravity waves, where the crests and throughs already show good contrast in the unfiltered images and smoothing would unnecessarily bias the results (see Section 4.2.1). As an example, Figure 3 compares the highest temporal resolution ($\Delta t = 1$ min) first and second time derivatives of channel 11 (8.4 μm) BT_{11} for a sunset scene in the GOES-17 M2 Samoa domain. The channel 2 (0.65 μm) visible radiances and BT_{11} itself are also plotted for context
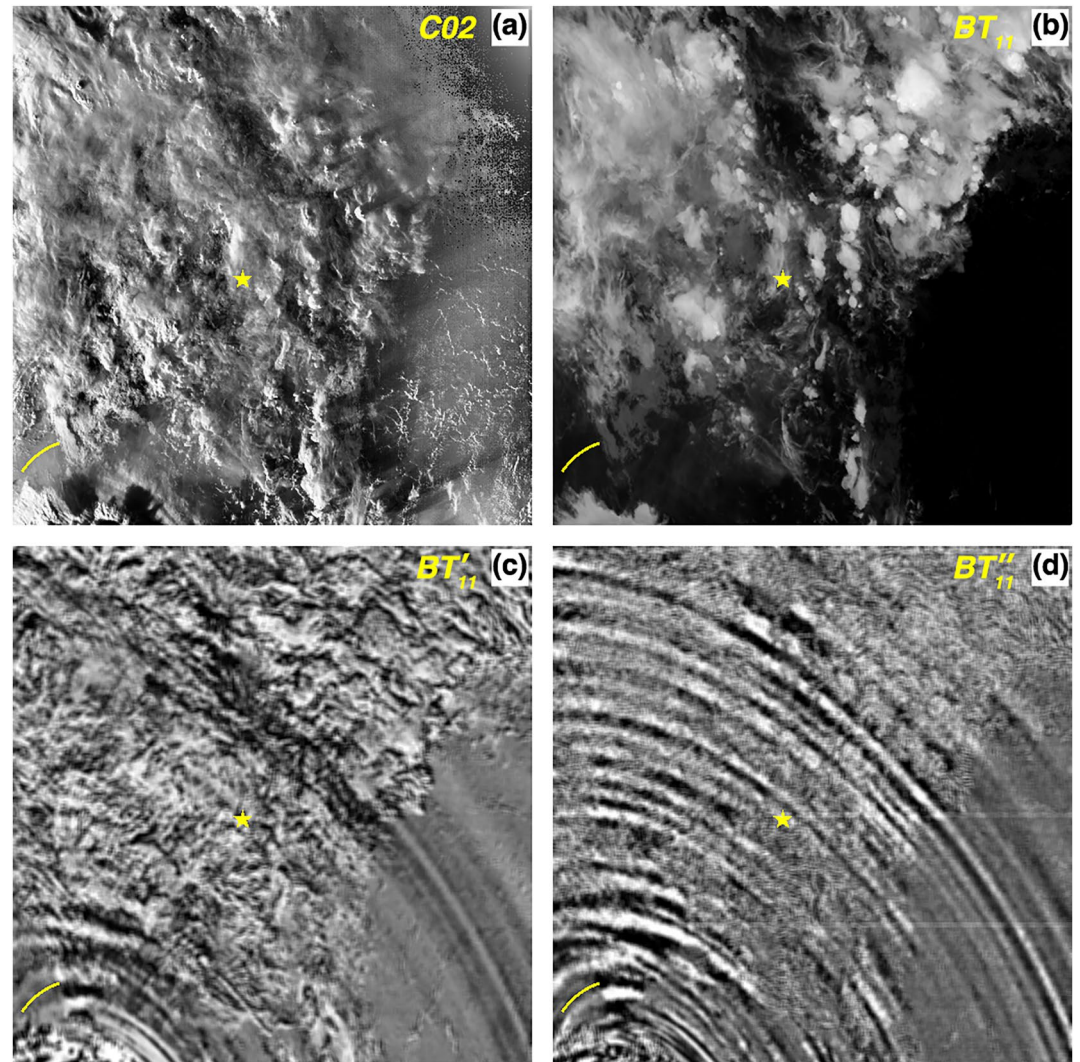
Figure 3. (a) Channel 2 (0.65 µm) visible radiances, (b) channel 11 (8.4 µm) brightness temperatures BT_{11}, (c) first time derivative BT'_{11}, and (d) second time derivative BT''_{11} in G17_M2 (Samoa) at 05:35 UTC on 15 January 2022. The visible image was enhanced by adaptive histogram equalization and BT_{11} was gray scaled between 190 K (white) and 290 K (black). The interval used for calculating the time derivatives is $\Delta t = 1$ min. The time derivative images were gray scaled over the respective ranges of ± 1 K min^{-1} and ± 0.25 K min^{-2}, histogram equalized, and mean filtered using a 5×5-pixel window. The yellow star marks the location of the Pago Pago pressure time series plotted in Figure 2. The yellow arc in the bottom left are clear pixels $\sim 341 \pm 2$ km from HTHH with a backazimuth of 320°–345°, the mean brightness temperature of which is plotted in Figure 5.

in Figures 3a and 3b, respectively. Most of the domain is covered with clouds, ranging from low-level ones to deep convection. In the bottom left corner of Figure 3a, the stratospheric plume from the main eruption intrudes into the domain and casts a shadow on lower-level clouds. The right and bottom third of the domain are warm ocean peppered only with small popcorn cumuli and, hence, show high BT_{11} (black areas in Figure 3b).

The concentric arcs of waves emanating from HTHH are partially visible in BT'_{11}, especially over mostly clear ocean (Figure 3c). However, the waves are still difficult to discern in thicker clouds, where large temperature fluctuations due to horizontal or vertical cloud motion mask the small eruptive temperature anomalies. This complicating background is greatly diminished in BT''_{11}, which enhances the spatially coherent signal from fast propagating waves (Figure 3d). The second time derivative collates information from three images and, thus, works better than the first time derivate, which is based on two images. The BT''_{11} field reveals a multitude of closely spaced wave crests and troughs, even in cloudy areas. Due to its obvious superiority, we use the second time derivative of brightness temperatures for most subsequent analysis.

The emergent pattern of alternating brighter and darker arcs is insensitive to the type of finite difference scheme. Replacing the central differences in Equation 2 with forward or backward differences leads to a pattern that is shifted slightly forward or backward in the radial direction, but otherwise shows the same fine-scale band structure.

The concentric waves in Figure 3d can be easily followed from clear ocean over to high-level clouds without a noticeable dislocation in the arcs at the clear-cloudy interface and are also present in all IR channels, pointing to Lamb waves that span the full depth of the troposphere. Channel differences are further demonstrated in Supporting Information S1 (Figures S2 and S3).

Of the earlier studies, Wright et al. (2022) used the first time derivative, while Amores et al. (2022), Matoza et al. (2022), Otsuka (2022), and Winn et al. (2023) used the second time derivative of brightness temperatures to identify waves. However, all previous studies were based on full-disk imagery with a significantly longer sampling period of $\Delta t = 10$ min for GOES-R and Himawari-8 and $\Delta t = 15$ min for Meteosat. The consequences of such reduced temporal sampling are discussed in Section 3.6.

3.3.2. Spatial Fourier Filtering

Although the used boxcar averaging already constitutes a low-pass spatial filter, additional spatial filtering can be applied to the data to improve the detection of the dominant wave signature. The BT'' images are converted by a fast Fourier transform (FFT) into the frequency domain, in which an ellipsoidal filter removes certain high-wavenumber components and then the result is transformed back into the spatial domain by the inverse FFT.

Figure 4 demonstrates FFT filters for the two main wave pattern types encountered in the mesoscale observations. In near-field domains, the dominant pattern consists of concentric circles or arcs (Figure 4a). Here we note that
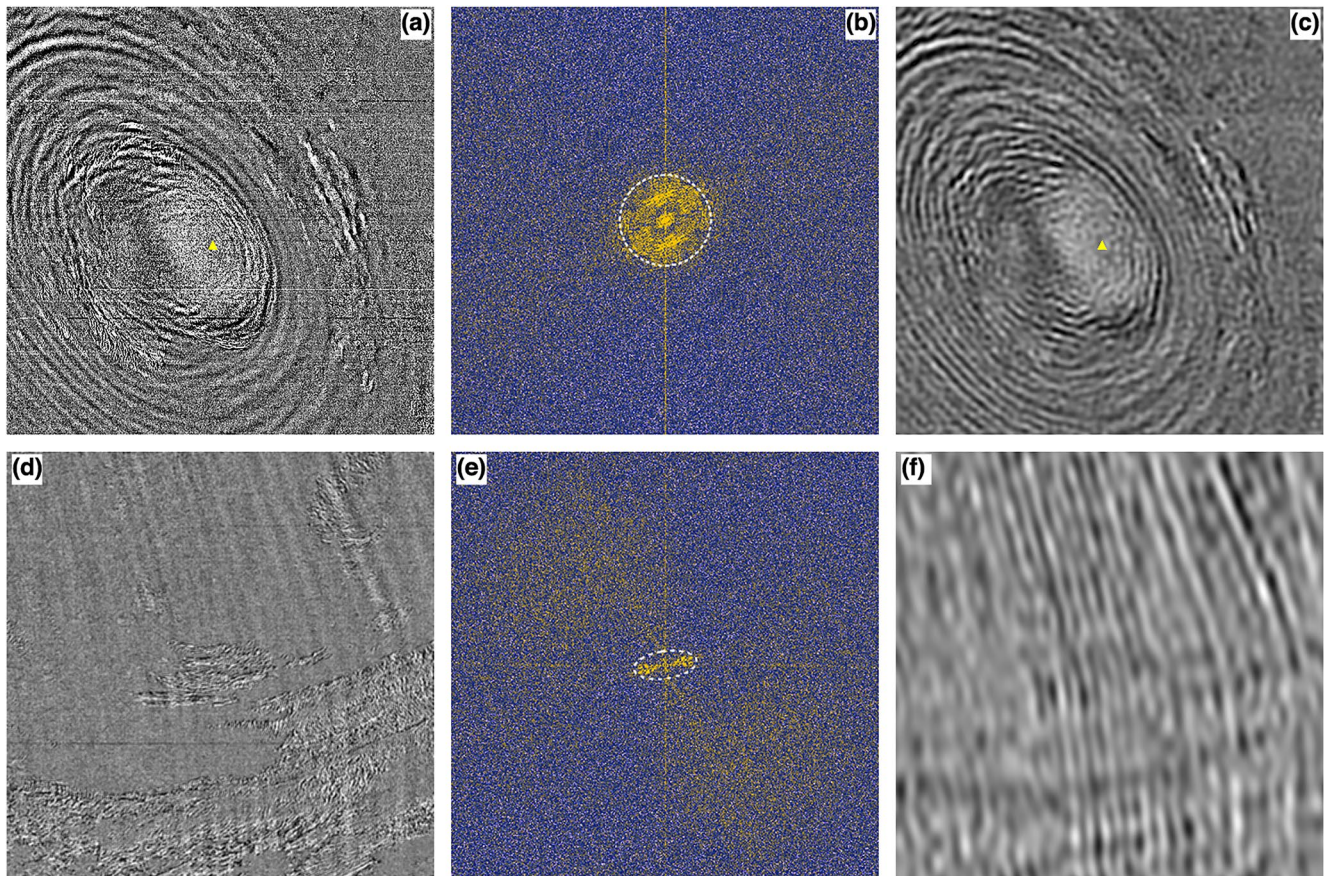

Figure 4. Examples of low-pass FFT filtering of BT''_{12} (9.6 μm): (top row) concentric circles in the near-field G17_M1 HTHH domain (HTHH marked by the yellow triangle) at 07:15 UTC on 15 January 2022 and (bottom row) meridional bands in the far-field G16_M2 domain (Texas) at 13:35 UTC on 15 January 2022. The interval used for calculating the time derivative is $\Delta t = 1$ min (a), (d) Raw grayscale image. (b), (e) Log of the 2D spatial power spectrum. The filter only keeps frequencies within the white dashed circle/ellipse. (c), (f) Spatial frequency-filtered image.

the vertical near-side perspective view (fixed grid image) is a non-conformal projection in which angles and shapes are distorted; thus, circles appear as ellipses away from the subsatellite point. In far-field domains, the characteristic pattern is a train of bands, whose orientation (slope) depends on the domain's geographic location relative to HTHH (Figure 4d).

The 2D spatial power spectrum (Figures 4b and 4e) is zeroed outside of an ellipsoidal mask to reduce high-frequency variations, noise, and striping. Instead of using a fixed mask, we subjectively adjust the size and rotation of the ellipse per domain, such that it emphasizes the dominant wave patterns (Figures 4c and 4f). The animations given in the Supporting Information demonstrate the filter adjustment.

In our experience, low-pass FFT filtering might not significantly enhance the visual perception of waves in individual static images. Nevertheless, it always helps detecting the passage of waves and estimating their phase speed in the time–distance plots (or keograms) we introduce in Section 4.1.

3.4. The Primary Lamb Wave in BT

As discussed earlier, detecting the HTHH-induced absolute temperature perturbations on a pixel-by-pixel basis is difficult, because the typical spatiotemporal variations in BT due to tropospheric dynamics usually mask the signal. However, it is possible to extract the mean signature of the long-period primary wave in certain cloud-free areas, where the background temperature remains relatively steady without large fluctuations. The yellow arc in Figure 3 marks such a set of mostly clear pixels, which are ~341 ± 2 km from HTHH with a backazimuth of 320°–345°. Assuming a wave velocity of ~315 m s^{-1}, these pixels are ~18 min downstream from HTHH and ~26 min upstream from Pago Pago (indicated by the yellow star).

Figure 5a plots the 1-min resolution temporal variation of the mean BT_{12} over the arc between 03:58–05:58 UTC. We use the ozone channel 12, because it is less sensitive to clouds due to its weighting function peaking in the stratosphere. A wave with an amplitude of ~5 K and period of ~30 min is apparent in the mean temperature. The 04:51 UTC and 05:20 UTC maxima in the mean BT_{12} correspond to the 05:14 UTC and 05:46 UTC pressure peaks measured downstream in Pago Pago (see Figure 2a).

A similar ~30 min-period temperature variation corresponding to the main Lamb pulse is also detectable in the far-field G16_M2 Texas domain. Figure 5b depicts the temporal variation of BT_{12} averaged over a subset of clear pixels (~9,974 ± 2 km from HTHH with a backazimuth of 49°–54°) between 12:00 and 14:00 UTC. Here the HTHH-induced temperature perturbations are superimposed on a generally decreasing background BT and have an order of magnitude smaller amplitude of only ~0.3 K.
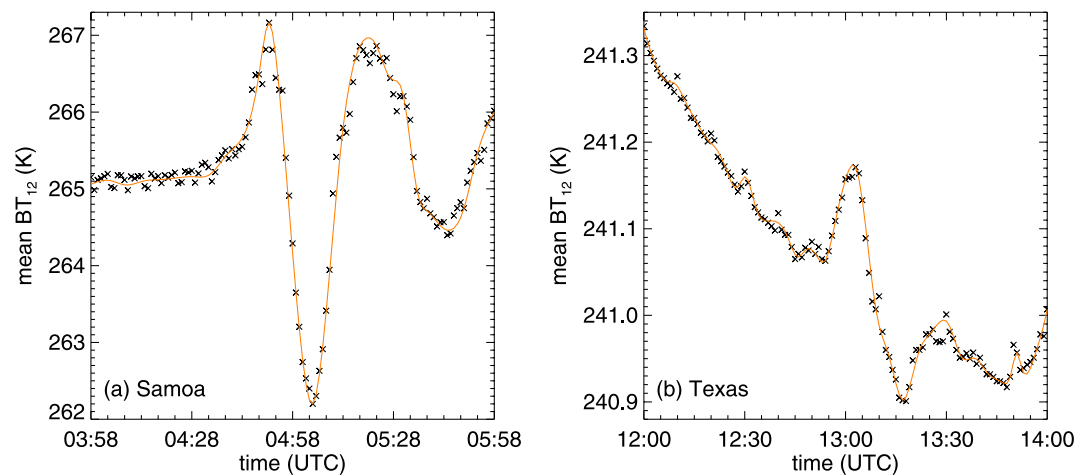

Figure 5. Time series of mean BT_{12} calculated for a set of clear pixels in (a) G17_M2 Samoa domain (yellow arc in Figure 3) and (b) G16_M2 Texas domain (pixels ~9,974 ± 2 km from HTHH with a backazimuth of 49°–54°). The orange cubic spline fit is plotted merely as visual guide.
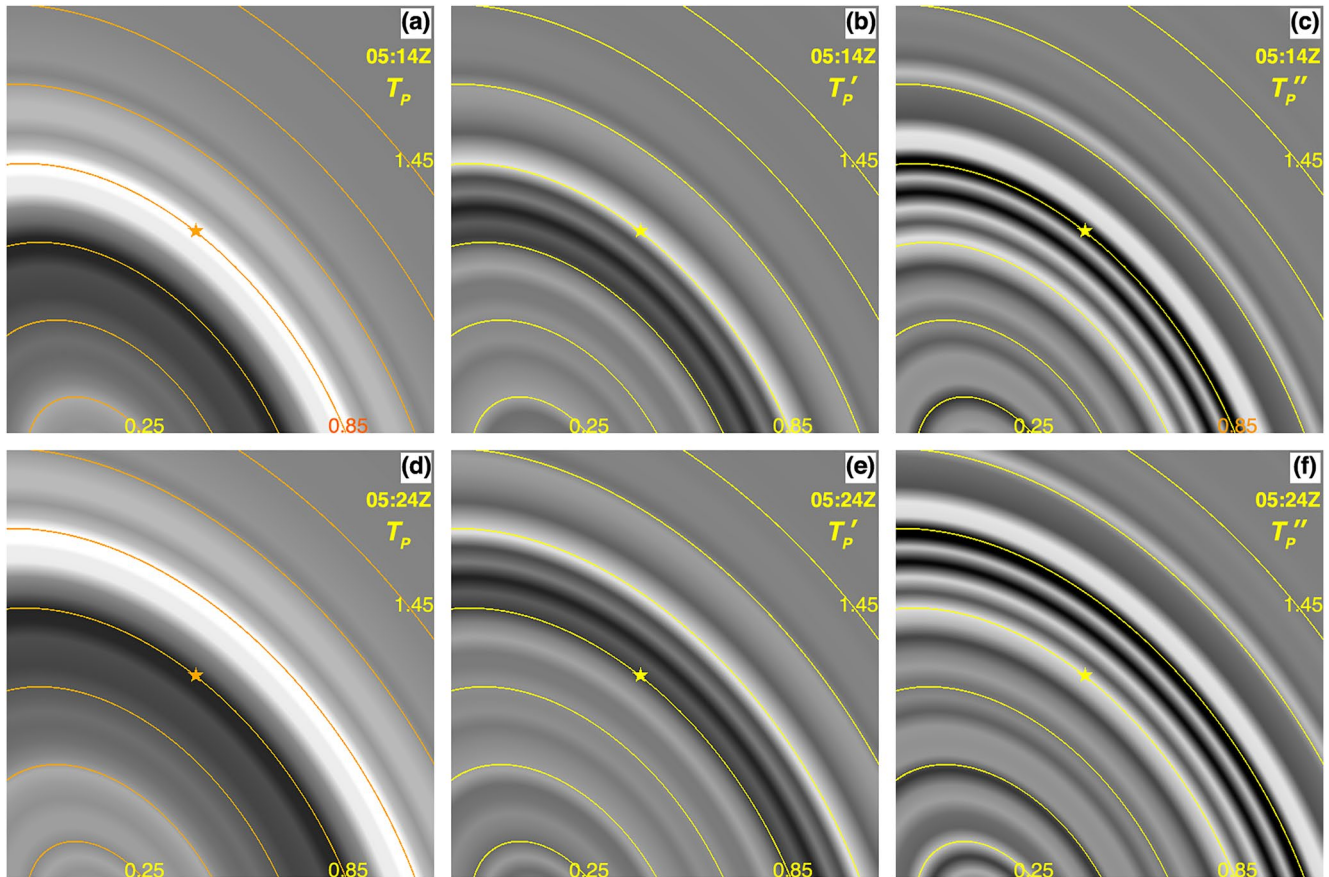
Figure 6. Temperature anomaly waveform and its time derivatives modeled on the Pago Pago pressure anomaly waveform and propagated through the G17_M2 Samoa domain, at (top row) 05:14 UTC and (bottom row) 05:24 UTC on 15 January 2022. (a), (d) Temperature anomaly T_P gray scaled between ± 1 K (white to black). (b), (e) First derivative T_P'. (c), (f) Second derivative T_P''. The star marks Pago Pago and the orange or yellow lines are isodistances ($\times 1{,}000$ km) from HTHH drawn at 200 km intervals.

3.5. A Simple Model of the Temperature Wave Packet

As discussed previously, the pressure waveform can be used as a first-order model of the temperature waveform, especially in the nearest Samoa domain, where the pressure signal is robust. We devise temperature anomalies by linearly scaling the 2-min pressure anomalies in Figure 2a such that the peak-to-trough amplitude becomes 2 K (+1.3 K at 05:14 UTC and −0.7 K at 05:24 UTC). The amplitude of the temperature anomaly generally decreases with distance from HTHH and also depends on altitude and channel. We show later that the amplitude of the mean temperature anomaly reconstructed from the observed window channel *BT* time derivatives is ~2 K at the isodistance of Pago Pago. Such a *BT* perturbation is representative of the cloudy regions dominating our scene, but it is an overestimate in clear sky regions. In the latter, the peak-to-trough temperature amplitude is only 0.5–1.0 K, as estimated by Otsuka (2022) for an isothermal atmosphere and adiabatic pressure change.

This synthetic cloud-level temperature waveform T_P is propagated through the G17_M2 Samoa domain assuming isotropic spreading with a speed of 315 m s^{-1}. The waveform derivatives are then calculated and processed as described in Sections 3.2 and 3.3.

Movie S1 in Supporting Information S1 shows the propagation of the modeled temperature anomaly waveform and its derivatives between 03:58 and 05:58 UTC. Snapshots corresponding to the passage of the maximum positive and negative temperature anomaly over Pago Pago are plotted in Figure 6.

At 05:14 UTC, the broad bright band in the T_P image along Pago Pago's isodistance (850 km) represents the primary peak of the wave packet (Figure 6a). The two fainter bands downstream correspond to the two smaller preceding peaks of the waveform. The darkest band ~200 km upstream (650 km isodistance) is the trough of the

main Lamb pulse, which reaches Pago Pago at 05:24 UTC (Figure 6d). The full ∼50 min wave packet is confined between the 250–1,250 km isodistances in Figure 6a and between the 450–1,450 km isodistances in Figure 6d (the packet moves ∼190 km per 10 min).

The first derivative of the temperature perturbations T_P' shows a larger number of thinner bands, as it highlights the temperature tendency within the packet. The bright band along Pago Pago's isodistance at 05:14 UTC marks the largest temperature increase at the peak of the main pulse (Figure 6b). In contrast, the dark band passing Pago Pago 10 min later represents the steepest temperature drop at the trough of the main pulse (Figure 6e). The broad long-period variation in temperature, however, cannot be identified in this representation.

The second derivative of the temperature perturbations T_P'' visualizes the fine-scale variations the sharpest, as it represents the local concavity of the waveform. Its sign is usually opposite of T_P' for our particular waveform. Along Pago Pago's isodistance, T_P'' is negative at 05:14 UTC (dark band in Figure 6c) and positive at 05:24 UTC (bright band in Figure 6f), because the waveform is concave down near the peak and concave up near the trough of the main Lamb pulse. The long-period temperature variation is not visually encoded in T_P'' either, because concavity is generally uncorrelated with the magnitude of the temperature anomaly.

In real world data, the temperature waveform is superimposed on a spatiotemporally highly variable background. To mimic this, we simply add the modeled temperature perturbation T_P to actual BT_{11} imagery obtained before the eruption. Recall that mesoscale imagery in the G17_M2 Samoa domain is available between 02:41 and 05:59 UTC on 15 January and the first visually detectable wave only appears at 04:16 UTC. Thus, imagery prior to 04:16 UTC do not contain the HTHH wave signature and can be safely combined with the T_P shown in Figure 6.

Movie S2 in Supporting Information S1 shows such "simulated" cloudy BT_{11} imagery, its second time derivative, as well as the second time derivative of the actually observed BT_{11}. The 05:14 UTC and 05:24 UTC snapshots of the simulated and observed waveform derivatives are plotted in Figure 7. Note that the cloud patterns are at slightly different locations in the simulated and observed images, because the former depicts the cloud field at an earlier time than the latter.

Unlike against a uniform background as in Figure 6, the passage of the temperature perturbations cannot be discerned against a natural cloudy background (see Movie S2 in Supporting Information S1). The second derivative of the simulated brightness temperatures, however, well describes that of the observed ones. The sequence, width, and location of the bright and dark arcs of the observed and simulated waveform derivatives are in excellent agreement—the contrast variations of the simulated patterns are, however, overemphasized in clear sky areas, because the imposed cloud-level temperature anomalies are excessive in cloud-free regions. The only exception is the bottom left corner of the domain, where the observations show a larger number of shorter period wave fronts. It is here where the stratospheric umbrella of the HTHH plume intrudes the domain and hence the satellite observations are likely dominated by gravity waves. Unlike Lamb waves, which extend through the entire troposphere, these high-altitude gravity waves cause no measurable anomalies in the Pago Pago surface pressure on which our assumed temperature perturbations are based; thus, gravity waves are missing from the simulated images.

As demonstrated, the pressure perturbations explain the salient features of the temperature waveform derivatives visualized in the satellite imagery. The relationship between the pressure and temperature perturbations, however, can be further quantified. The orange curves in Figures 2b and 2c depict the observed (real) temporal variation of the first and second derivative of BT_{13} at Pago Pago–here the temperature derivatives were averaged along the 850-km isodistance to reduce noise. The temperature and pressure waveform derivatives match up excellently. The correlation between P' and BT_{13}' is 0.9 and that between P'' and BT_{13}'' is 0.94 for the entire 2-hr period. The slightly lower correlation between the first derivatives is due to natural temperature variations in the 4–5 UTC period before the arrival of the eruption's pressure wave. In the post-arrival period of 5–6 UTC, both the first and second derivatives correlate at 0.94.

Finally, the temperature perturbations can be approximately reconstructed from the measured BT time derivatives by recursively applying the inverse of the finite difference operators in Equations 1 and 2 (antidifference operator). The reconstruction is unique up to an additive constant when using the first derivatives and up to an additive linear trend when using the second derivatives.
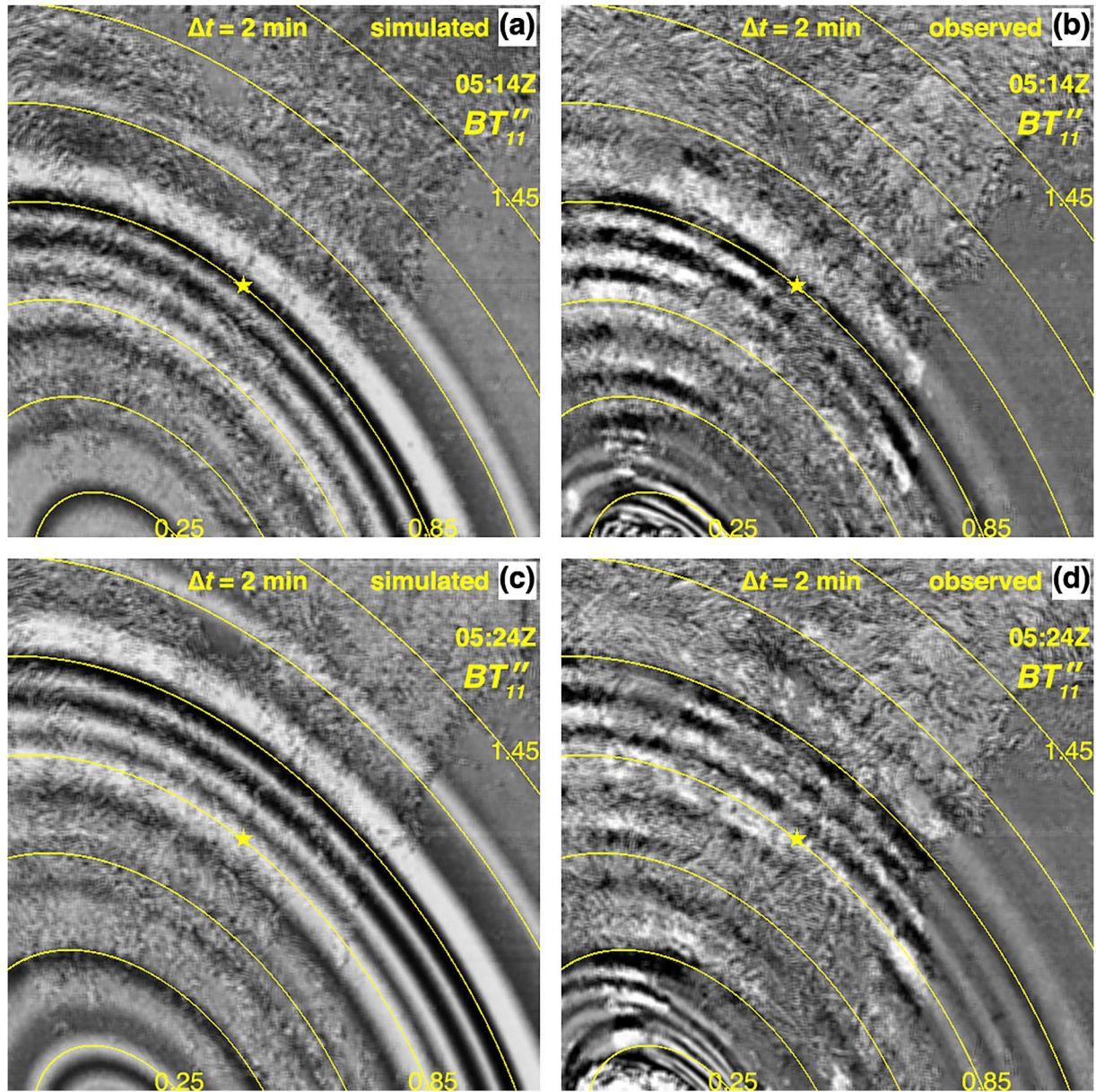
Figure 7. Second time derivative BT''_{11} visualized against a cloudy background: (a), (c) simulated and (b), (d) observed in the G17_M2 Samoa domain at (top row) 05:14 UTC and (bottom row) 05:24 UTC on 15 January 2022. The simulated images combine the modeled temperature anomalies in Figure 6 with pre-eruption BT_{11} images that were obtained 77 min earlier than the actual observation time of the waves indicated in the panels. The star marks Pago Pago and the yellow lines are isodistances ($\times$1,000 km) from HTHH drawn at 200 km intervals.

The orange curve in Figure 2a depicts the BT_{13} anomalies reconstructed from the mean BT''_{13} plotted in Figure 2c. Here, we started the recursion at 5 UTC and removed a linear trend from the reconstructed temperature anomalies—the observed mean BT_{13} for Pago Pago's isodistance also increased between 5 and 6 UTC, unrelated to the eruption. As shown, the reconstructed mean temperature anomaly waveform has a peak-to-trough amplitude of ~2 K and correlates well with the observed surface pressure waveform with a coefficient of 0.94.

The corresponding results for Δt = 10 min sampling are given in Figures 2d and 2f and 8. Both time derivatives of the subsampled temperature waveform show the familiar positive–negative–positive anomaly pattern of the main Lamb pulse found by previous studies using FD imagery. There is a slight asymmetry between the positive peaks. The first peak is larger and narrower than the second one for the first derivative, while the opposite is true for the second derivative where the second peak is somewhat larger.
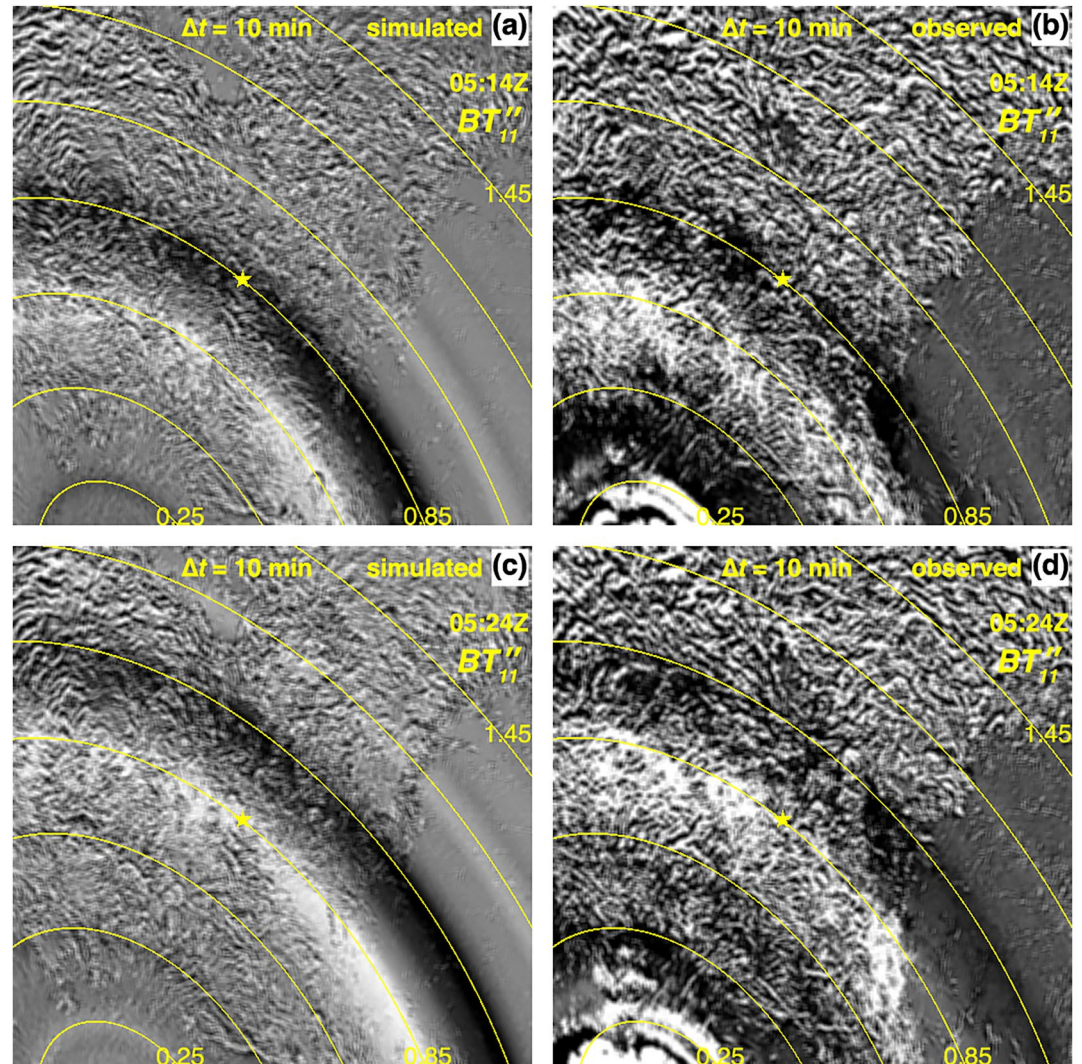
Figure 8. Same as Figure 7, but for Δt = 10 min sampling.

In FD imagery, these subsampled waveform derivatives manifest as bright–dark–bright bands of ~190–200 km width (the distance the acoustic wave packet travels in 10 min). Depending on the relative magnitude of the positive peaks, the cloud background, as well as the applied spatial smoothing and color saturation, sometimes only the single bright band of the larger peak is discernible. As before, the differences between the simulated and observed patterns in the bottom left corner of the domain are likely due to gravity waves in the stratospheric umbrella.

3.6. Spatiotemporal Aliasing

To summarize our results so far, the wave patterns seen in the imagery are determined by the interplay of two opposing effects. The time derivatives amount to a high pass filter, which highlights the shorter period fluctuations within the wave packet. Conversely, only the longer period variations are preserved when the observation frequency is reduced. In this section, we discuss the latter aliasing effect in more detail.

The minimum wavelength and wave period that can be captured in the satellite observations are determined by the spatiotemporal characteristics of the images and basic sampling theorem. The Nyquist–Shannon condition requires at least two samples per period (both spatial and temporal) for successful signal reconstruction. As discussed in Section 2, the typical grid spacing in most of the mesoscale domains is 3–6 km, depending on propagation azimuth and location in
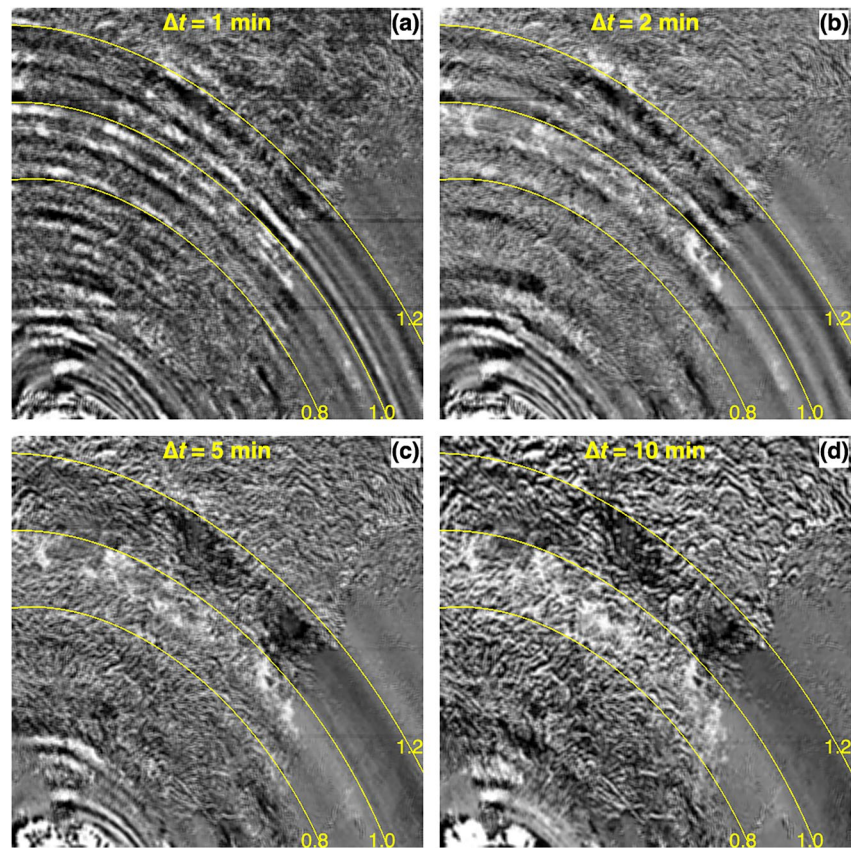
Figure 9. Near-field spatiotemporal aliasing in BT''_{11} in G17_M2 (Samoa) at 05:30 UTC on 15 January 2022. The interval used for calculating the time derivative is (a) $\Delta t = 1$ min, (b) $\Delta t = 2$ min, (c) $\Delta t = 5$ min, and (d) $\Delta t = 10$ min. The images were histogram equalized and mean filtered using a 5×5-pixel window. The yellow lines are isodistances ($\times 1,000$ km) from HTHH.

the domain. This translates to a minimum observable horizontal wavelength of 6–12 km. In the GOES-17 M2 Alaska domain the minimum observable wavelength is larger, $\sim$16–20 km, due to the reduced image resolution near the limb. The maximum detectable wavelength, on the other hand, is equal to the domain size or $\sim$1,000 km.

Similarly, the 1-min sampling period of the mesoscale scans corresponds to a minimum resolved wave period of 2 min, or a maximum resolved frequency of 8.3 mHz. All higher frequency variations are aliased to lower frequencies. The temporal aliasing (or under-sampling) artifact is significantly more severe in the lower cadence full disk imagery. The shortest period and highest frequency that can be resolved in GOES-R and Himawari-8 FD with a sampling period of 10 min are 20 min and 0.83 mHz, respectively, while these cutoffs are 30 min and 0.56 mHz for Meteosat FD with a sampling period of 15 min.

Microbarometer measurements reported by Matoza et al. (2022) indicate that the HTHH eruption generated infrasound (>10 mHz) as well as audible sound (>20 Hz), which are above the Nyquist frequency of the mesoscale scans. Johnson et al. (2023) demonstrated that infrasonic waves in volcanic plumes are detectable by high frame-rate video obtained in the immediate vicinity of the vent. The amplitude of these higher-frequency waves, however, is too small to cause noticeable perturbations in satellite observations. The satellite brightness temperatures contain information about Lamb waves and gravity waves instead.

Figure 9 demonstrates the effect of longer sampling periods on the wave patterns that emerge in the near-field BT'' images. The results for the shortest sampling period of $\Delta t = 1$ min are compared with those for longer periods of $\Delta t = 2$, 5, and 10 min, which cover the typical sampling rates of operational geostationary imagers: Himawari-8 rapid scan, Meteosat rapid scan, and GOES-R and Himawari-8 full disk scan, respectively.

The highest temporal resolution data reveal a swarm of densely packed concentric waves with the main pulse near the 1,200 km isodistance (Figure 9a). The waves propagate with a speed of $\sim$315 m s^{-1} as we show in Section 4.1. Their horizontal wavelength increases from $\sim$40 to 50 km to $\sim$50–70 km with distance from HTHH. The increase
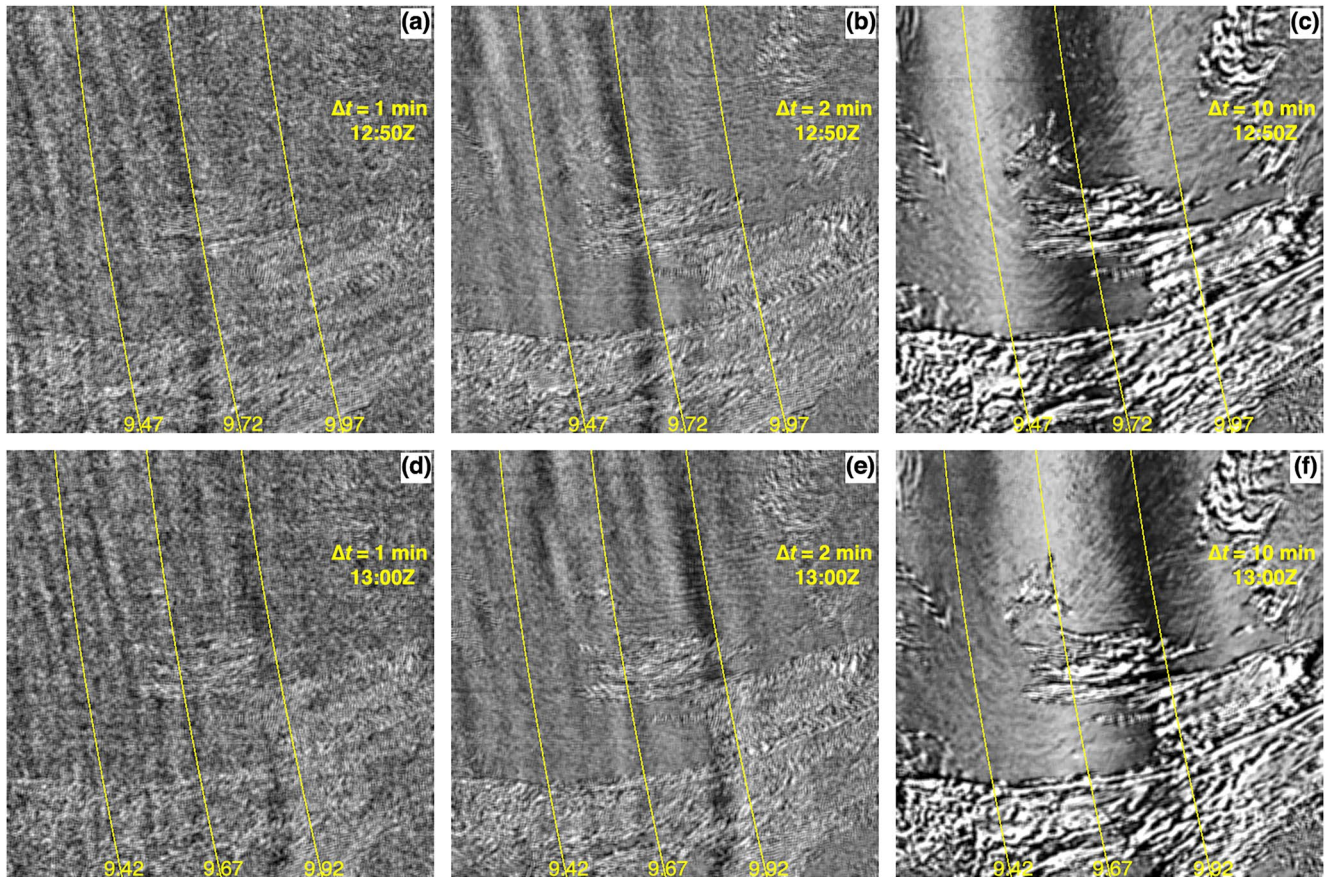
Figure 10. Far-field spatiotemporal aliasing in BT''_{12} in G16_M2 (Texas) at (top row) 12:50 UTC and (bottom row) 13:00 UTC on 15 January 2022. The interval used for calculating the time derivative is (a), (d) $\Delta t = 1$ min, (b), (e) $\Delta t = 2$ min, and (c), (f) $\Delta t = 10$ min. The images were histogram equalized and mean filtered using a 5×5-pixel window. The yellow lines are isodistances ($\times 1,000$ km) from HTHH.

in λ_H across the domain might be due to dispersion—longer waves traveling faster—caused by vertical and horizontal variations in wind and temperature (Garrett, 1969). Alternatively, it could be due to the emission of several individual wave packets. There were multiple explosions between 4 and 6 UTC (see Figure 2a), which could have different horizontal extent, leading to different characteristic λ_H.

As the sampling period gets longer, the fine detail in the BT time derivatives is gradually lost (Figures 9b-9c-9d). This is the manifestation of spatiotemporal aliasing, where frequencies above the Nyquist frequency of the given sampling rate become aliased to lower frequencies and longer wavelengths, resulting in an effect resembling "motion blur". Some loss of detail is already noticeable for $\Delta t = 2$ min, but for full disk sampling with $\Delta t = 10$ min, the observed pattern is reduced to ~200 km wide dark and bright bands as shown previously in Figure 8.

The aliasing in a far-field domain is depicted in Figure 10. At high frequency sampling ($\Delta t = 1$ or 2 min), the main Lamb pulse is represented by the dark band near the 9,720 km isodistance in the 12:50 UTC image. There is a fainter dark band ~120–140 km ahead (east) of the main pulse, which corresponds to the smaller pressure peak emitted ~7 min earlier (see Figure 2a and Figure S1 in Supporting Information S1). Here we note that Vadas, Figueiredo, et al. (2023) analyzed 4.3-μm BT perturbations in an Atmospheric Infrared Sounder (AIRS) granule over Antarctica (7,500–8,000 km from HTHH). They found a Lamb amplitude peak at a wavelength of ~146 km, which agrees with our finding for the distance between the main pressure peak and the preceding one.

The main pulse is followed by a long train of waves with wavelengths decreasing in time from ~65 to 75 km to ~40–50 km, which again suggests dispersion. Full disk sampling ($\Delta t = 10$ min) only reveals the primary pulse, with the dark and bright bands having an increased width and wavelength of ~250 and ~500 km, respectively,
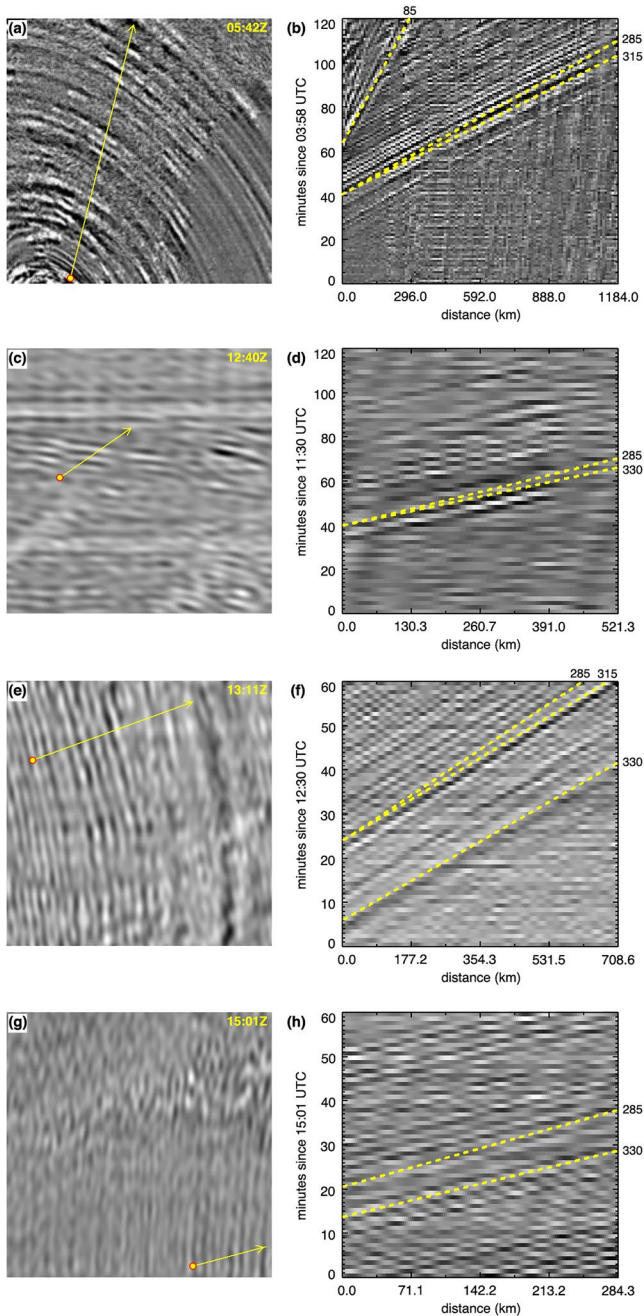
Figure 11. Passage of A1 waves across the mesoscale domains on 15 January 2022. From top to bottom: (a), (b) G17_M2 (Samoa) 03:58–05:58 UTC, C11, (c), (d) G17_M2 (Alaska) 11:30–13:30 UTC, C11, (e), (f) G16_M2 (Texas) 12:30–13:30 UTC, C12, and (g), (h) G16_M1 (Alabama) 15:01–16:01 UTC, C09 (6.9 μm). The left panels are snapshots of BT'' at the indicated times and the right panels are time–distance plots over one- or 2-hr periods with guides of constant phase speed drawn (dashed yellow, in m s^{-1}). The yellow arrows are aligned with fixed back-azimuths and indicate the overall propagation direction. Distance is measured from the circle (0 km) toward the arrowhead. The interval used for calculating BT'' is $\Delta t = 2$ min for G17_M2 (Alaska) and $\Delta t = 1$ min otherwise. Except for the top row, the BT'' images were FFT-filtered.

compared to the near field. The waves travel with a slightly larger observed propagation velocity of ~330 m s^{-1}, which likely is due to the added effect of westerly winds in this domain.

4. Far-Field Lamb Waves and Near-Field Gravity Waves

4.1. Minor Arc and Major Arc Passage of Lamb Waves

In this section, we track the first minor arc (A1, from west to east toward the antipode) and major arc (A2, from east to west toward HTHH) passage of the waves across the mesoscale domains on 15 and 16 January 2022, respectively. The third and fourth passages are also weakly detectable in the data, but we focus on the stronger and more informative signature of the first two passages. The ground-based propagation speed of the waves is estimated with the help of time–distance plots introduced in Figure 11. A time–distance plot is constructed by stacking 1D slices of the BT'' images taken along a path marked by the yellow arrow. The path is aligned with a fixed back-azimuth and indicates the overall propagation direction. In such a stack plot, wave crests and troughs traveling along the path are represented by bright and dark stripes, whose slope encodes the propagation speed. With distance on the x-axis and time on the y-axis, the slope decreases with increasing speed.

For simplicity, we use line segments as paths, which, nevertheless, are well aligned with geodesics over the mesoscale distances considered here. Due to the spatial (pixel) discretization, the speed estimates are virtually insensitive to a 5°–10° variation in the back-azimuth of the segment.

The longer the line segment, however, the better the separation of stripes corresponding to different speeds. The longest possible segment is the domain's diagonal, which is ~2,000 km for the near-field and ~1,500 km for the far-field domains. In practice, however, the length of the line segment available for tracking is significantly shorter, because the waves are visible only in certain parts of the domain. In our case, the length of segments used for speed estimation ranges between ~300 and 1,200 km. Over such distances, the travel time difference between speeds of 285 m s^{-1} and 315 m s^{-1} varies from 1.7 min to 6.7 min. These travel time differences correspond to a mere 2–6 or 1–3 tick mark separation along the y-axis for $\Delta t = 1$ min and $\Delta t = 2$ min sampling, respectively. Thus, a variation of 30 m s^{-1} (or 10%) around the sound speed is slightly or just barely distinguishable in the mesoscale data, depending on the length of the segment and the sampling period. This uncertainty should be kept in mind when interpreting the stack plots.

The initial passage of A1 waves across the GOES-17 M2 Samoa domain between 04:00 and 06:00 UTC on 15 January is shown in Movie S3 in Supporting Information S1 and Figures 11a and 11b. The first visually detectable wave appears at the bottom of the domain ~170 km from HTHH at 04:16 UTC. The time–distance plot reveals the passage of more than a dozen wave crests during this 2-hr period. The observed speed clearly exceeds the GW speed limit of ~285 m s^{-1} (see Extended Data Figure 6 in Wright et al., 2022) and is estimated at ~315 m s^{-1}. This velocity combined with the arrival time puts the emission time of the first wave at ~04:07 UTC, which agrees with the time of the first eruptive event in the Samoa surface pressure (Figure 2a) as well as in distant infrasound
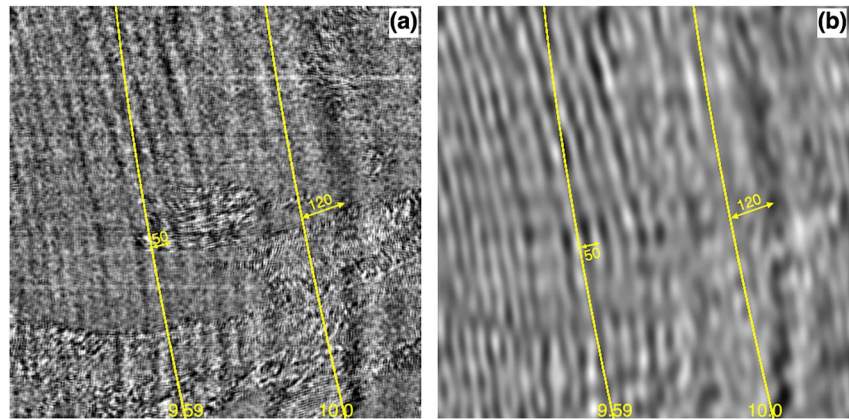
Figure 12. Anisotropic wave propagation in G16_M2 (Texas): (a) raw grayscale image and (b) FFT-filtered image of BT''_{12} at 13:11 UTC on 15 January 2022. The interval used for calculating the time derivative is $\Delta t = 1$ min. The yellow lines are isodistances ($\times 1{,}000$ km) from HTHH, which were fitted to the bottom (southernmost) part of the thickest dark band (at 10 k km) and one of the thinner white bands (at 9.59 k km). The width of the dark band is ~50 km, while that of the white band is ~25 km. The maximum deviation of the midline of the wave bands from the fitted isodistances is also indicated (~120 and ~50 km, respectively).

and seismo-acoustic records (Matoza et al., 2022). The wave fronts follow isodistances very well, indicating isotropic propagation in the near field.

The horizontal wavelength tends to increase from ~40 to ~70 km with increasing distance from HTHH (period 2.1–3.7 min, frequency 4.5–7.9 mHz), suggesting some dispersion. The corresponding relatively small variations in speed, however, cannot be clearly detected given the uncertainty of our estimation method. The steeper stripes in the top-left corner of the stack plot represent slower GWs traveling with a speed of ≤ 85 m s^{-1}, which appear in the stratospheric umbrella cloud as it intrudes into the domain after ~05:00 UTC.

Tracking the waves in the near-limb GOES-17 M2 Alaska domain is more difficult due to the coarse pixel size and considerable horizontal striping. To increase the signal-to-noise ratio (SNR), we used $\Delta t = 2$ min sampling and applied FFT filtering to the images when constructing the stack plot (Movie S4 in Supporting Information S1 and Figures 11c and 11d). The waves are first visible near the bottom left (southwest) corner of the domain at ~11:15 UTC. Waves with longer $\lambda_H \approx 90$–110 km enter first, followed by waves with somewhat shorter $\lambda_H \approx 70$–90 km. The wavelength of subsequent waves cannot be estimated with confidence. Here, a propagation speed of ~330 m s^{-1} is a marginally better fit than the previously estimated ~315 m s^{-1}, at least for the longer wavelength waves that produce the clearest signal. Note that audible sound was reported at Kenai, Alaska between 13:15 and 13:45 UTC (Matoza et al., 2022), which is at the end of the 2-hr period when the passage of the wave train was detectable in the mesoscale data.

As the waves travel eastward, they enter the GOES-16 M2 (Texas) domain at ~12:20 UTC (Movie S5 in Supporting Information S1 and Figures 11e and 11f). The main Lamb pulse is detected first, followed by waves with a λ_H that generally decreases in time from ~75 to ~40 km (frequency 4.2–7.9 mHz). Waves can be observed in this domain at least until 15:00 UTC. Here, wave dispersion is perhaps also borne out by the stack plot speed estimates. The main pulse appears to propagate at a speed of ~330 m s^{-1}, while the traces of later wave fronts are better explained by a reduced speed of ~315 m s^{-1}. These waves are likely Lamb waves, because they travel faster than the absolute maximum GW speed limit of ~285 m s^{-1}, which is too slow to fit the data.

Finally, the waves are observed in the bottom half of our easternmost GOES-16 M1 (Alabama) domain between 15:01 and 16:20 UTC (Movie S6 in Supporting Information S1 and Figures 11g and 11h). This domain misses the main pulse and only captures the subsequent shorter waves with $\lambda_H \approx 40$–55 km. Because the waves can be best tracked over a short line segment in the bottom right corner, speed estimation from the stack plot is relatively uncertain. The wave traces indicate a propagation speed between 315 and 330 m s^{-1}.

By the time the waves reach the continental US, the wave fronts exhibit small but noticeable deviations from the isodistances. As shown in Figure 12 for the GOES-16 M2 Texas domain, the wave fronts travel faster in the
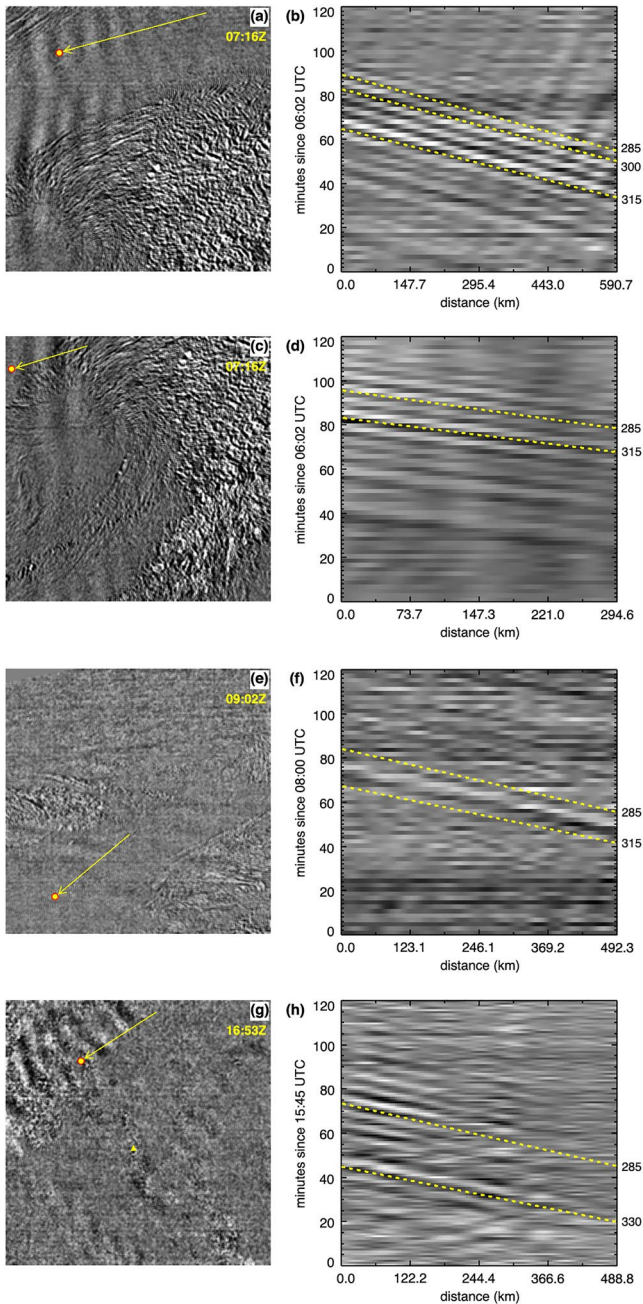
Figure 13. Passage of A2 waves across the mesoscale domains on 16 January 2022. From top to bottom: (a), (b) G16_M2 (Indiana) 06:02–08:02 UTC, C09, (c), (d) G16_M1 (Alabama) 06:02–08:02 UTC, C09, (e), (f) G17_M2 (Alaska) 08:00–10:00 UTC, C11, and (g), (h) G17_M1 (HTHH) 15:45–17:45 UTC, C07. The left panels are snapshots of BT'' at the indicated times and the right panels are time–distance plots over 2-hr periods with guides of constant phase speed drawn (dashed yellow, in m s^{-1}). The yellow arrows are aligned with fixed back-azimuths and indicate the overall propagation direction. Distance is measured from the circle (0 km) toward the base of the arrow. The interval used for calculating BT'' is $\Delta t = 1$ min for G17_M1 (HTHH) and $\Delta t = 2$ min otherwise. The snapshots in the left column are unfiltered images, while the time–distance plots in the right column are based on low pass-filtered images. The yellow triangle in panel (g) marks the location of HTHH.

middle than at the top or bottom of the domain (see also Figures 10 and 11e). The maximum deviation is ~120 km for the main Lamb pulse and ~50 km for the shorter-wavelength trailing waves. If we assume that the main pulse was emitted at ~04:29 UTC, the acquisition time and distance from HTHH lead to a mean propagation speed in the middle and at the bottom of the domain of ~323 m s^{-1} and ~319 m s^{-1}, respectively—in good agreement with the stack plot estimate of ~315 m s^{-1}. This ~4 m s^{-1} mean speed difference amounts to a remarkably small, ~1.3% anisotropy in propagation along paths that go over the US. In full-disk data, Wright et al. (2022) found larger deviations from isodistances in the portion of the main pulse which passed over the northern half of South America and slowed. The observed propagation anisotropy can likely be explained by temperature and wind variations as well as topography effects encountered along the travel path as argued by Sepúlveda et al. (2023) and Watada et al. (2023).

The A2 antipodal passage of the waves is shown in Figure 13 and Movies S7–S10 in Supporting Information S1. Because the signal becomes weaker during the longer major arc paths, we used $\Delta t = 2$ min sampling to increase the SNR. As before, the observed wavelength tends to decrease in time, suggesting wave dispersion. However, the visually detectable wavelengths shift toward larger values compared to the A1 passage and are typically within 95–120 km. The disappearance of shorter wavelengths is likely caused by the increased (acoustic) attenuation at higher frequencies.

The estimated propagation speed is in the range of 300–330 m s^{-1}. In the US domains, there is a hint of a slightly faster A1 passage (maximum ~330 m s^{-1}) than A2 passage (maximum ~315 m s^{-1}), which likely is due to the waves traveling with the midlatitude westerlies in the former case but traveling against them in the latter case. This observed speed reduction agrees with the modeling by Sepúlveda et al. (2023), which accounts for wind effects: the apparent phase speed decreases when the Lamb wave propagates against the wind and vice versa. Also note the complex interference patterns as the returning waves enter from different azimuths at different times and converge in the HTHH domain after circling the planet (Movie S10 in Supporting Information S1). Such complex far-field waveforms are produced and shaped by global wind variations.

4.2. Wave Phenomena Observed Over the Plume

So far, we have focused on far-field domains which did not observe the plume itself. The GOES-17 M1 domain, however, was moved to HTHH ~3 hr after the main eruption at 07:05 UTC on 15 January and remained there for 2 days. This domain allows us to study the generation and propagation of waves directly over the plume. Below we present three examples that demonstrate the potential of this data source. We focus on the first 2 hr of the data, because later imagery shows increased noise and striping, although waves are detectable at least until 14:00 UTC.

4.2.1. GWs Obscured by the Stratospheric Umbrella

A case when GWs are observed in the tropospheric umbrella but not in the stratospheric umbrella was captured during the first hour of the GOES-17 M1 HTHH data between 07:06 and 08:06 UTC (Movie S11 in Supporting Information S1). At that time the plume consists of two distinct layers, as
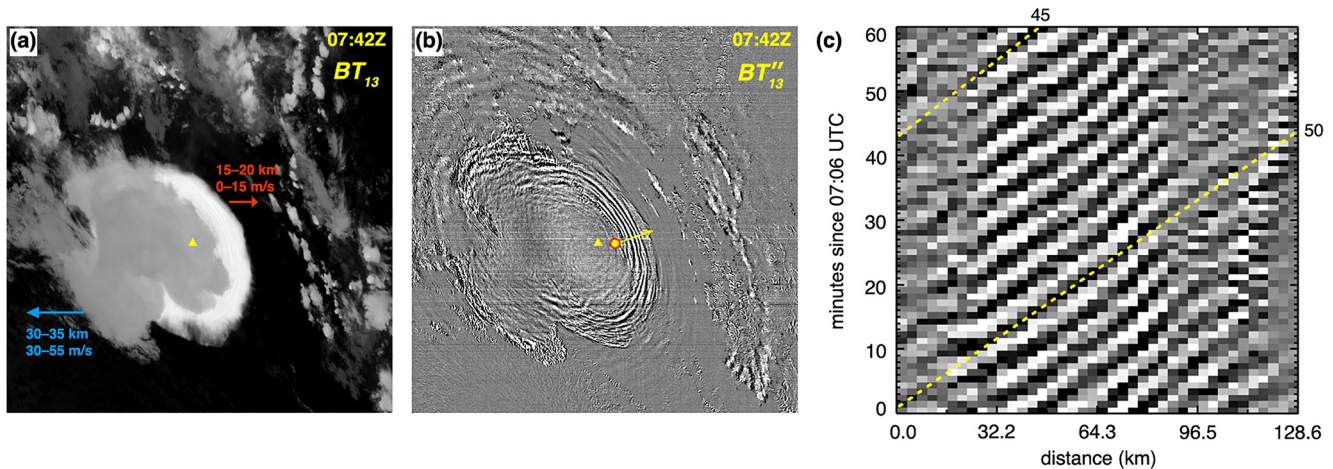
Figure 14. GW obscuration in G17_M1 (HTHH) on 15 January 2022: (a) channel 13 (10.3 μm) brightness temperatures BT_{13} at 07:42 UTC, (b) BT''_{13} at 07:42 UTC, and (c) time–distance plot for the period 07:06–08:06 UTC along the yellow arrow in panel (b). The interval used for calculating the time derivatives is $\Delta t = 1$ min. BT_{13} was gray scaled between 190 K (white) and 290 K (black), but no filtering was applied to BT''_{13}. The yellow triangle marks the location of HTHH. The height range and typical zonal velocity of the stratospheric and near-tropopause plumes are also indicated in panel (a).

shown by the 10.3 μm (band 13, "clean" longwave window) brightness temperatures in Figure 14a. The warmer stratospheric umbrella (~230 K, light gray) is located between 30 and 35 km, while the colder near-tropopause umbrella (~195 K, white) is spreading between 16 and 19 km. The eastward-propagating concentric arcs of short-wavelength GWs are clearly visible in the near-tropopause umbrella; however, their westward-propagating counterparts are absent from the stratospheric umbrella, as depicted by the BT''_{13} images in Figure 14b. The stack plot in Figure 14c indicates horizontal wavelengths of ~13–18 km and phase speeds of ~45–50 m s^{-1} (periods of ~4.8–6.0 min and frequencies of ~2.8–3.5 mHz). Note that at full-disk sampling ($\Delta t = 10$ min), these eastward-propagating short GWs seemingly move westward due to the wagon-wheel temporal aliasing effect (Movie S12 in Supporting Information S1).

If the source of these waves is below the tropopause, a potential explanation is critical level filtering. When the horizontal phase speed of upward propagating gravity waves equals the projection of the background wind speed along the GW propagation direction at a given altitude, the vertical component of group velocity approaches zero. At that critical level, the GWs are eliminated as their energy is absorbed and transferred to the background flow. This leads to the blocking of wave propagation in certain directions, depending on the wind profile.

A reanalysis mean wind profile is available from ERA5 (Hersbach et al., 2017; Figure S4 in Supporting Information S1), while actual plume motion and height retrievals were obtained by Carr et al. (2022) using stereo observations from Himawari-8 FD and GOES-17 M1 HTHH imagery. Both wind datasets show weak meridional winds typically between ±5 m s^{-1} throughout the entire troposphere and stratosphere. The zonal winds were eastwardly and relatively weak in the troposphere and near the tropopause; for the 16–19 km altitude range varying between 0 and 10 m s^{-1} in ERA5 and between 0 and 15 m s^{-1} with a mean of ~7 m s^{-1} in the stereo retrievals. Such weak winds have little effect on the eastward-propagating GWs detected in the lower umbrella.

In the mid stratosphere, however, the zonal winds were westwardly and much faster. In the 30–35 km altitude range of the upper umbrella, ERA5 indicates westward winds of 25–35 m s^{-1}. The stereo wind retrievals are significantly stronger, showing westward plume motion of 30–55 m s^{-1}. Thus, stratospheric plume motion is fast enough for critical level filtering to eliminate westward-propagating GWs emitted below the tropopause.

AIRS observations, however, show similar waves to the west of the volcano a few hours later (Wright et al., 2022). If the GWs are emitted in a region extending from the tropopause to the lower stratosphere, critical level filtering is unlikely to play a major role. The GWs might simply be obscured by the optically thick mid-stratospheric plume, which masks the BT perturbations.
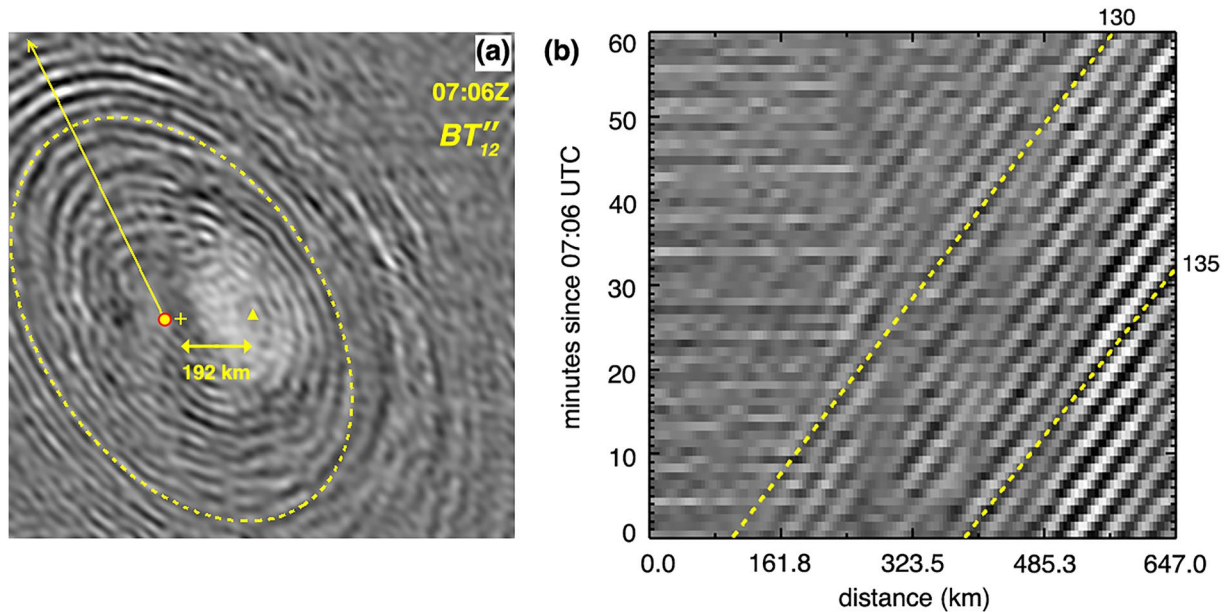
Figure 15. Mean flow advection in G17_M1 (HTHH) on 15 January 2022: (a) FFT-filtered BT''_{12} at 07:06 UTC and (b) time–distance plot for the period 07:06–08:06 UTC along the yellow arrow in panel (a). The interval used for calculating the time derivatives is $\Delta t = 1$ min. The yellow dashed curve is an ellipse fitted to one of the concentric rings with its center marked by the plus sign. The distance between the ellipse center and HTHH (yellow triangle) is also indicated.

4.2.2. Mean Flow Advection of GWs

Strong winds can horizontally shift the apparent center of concentric gravity waves, which was clearly demonstrated by the modeling study of Vadas et al. (2009). This effect is also observed in the first hour of the GOES-17 M1 HTHH data stream. Here we focus on faster GWs that are already noticeable in the northwestern (top left) corner of Figure 14b. These GWs, however, can be detected more clearly in the 9.6-µm "ozone" channel (C12), especially after FFT-filtering, as shown in Figure 15a (see also Movie S13 in Supporting Information S1). The vertical weighting function of C12 peaks at ~22 km, thus, the GWs are captured at a higher altitude, near the mid stratosphere, compared to the 10.3-µm window channel. The stack plot in Figure 15b indicates horizontal wavelengths of ~32–42 km and phase speeds of ~130–135 m s^{-1} (typical period of ~4.7 min and frequency of ~3.5 mHz). Note that this speed is essentially the theoretical maximum GW phase speed at this particular wavelength (see Extended Data Figure 6 in Wright et al., 2022).

It is evident in Figure 15a that the concentric rings cannot be fitted with ellipses centered on HTHH. A caveat to note is that the emission center of GWs in the satellite images is always shifted from HTHH, even in windless conditions, due to parallax. Because GOES-17 views HTHH from the east-northeast (azimuth of 66°) at a zenith angle of 50°, the apparent emission center is shifted to west-southwest (left and below) relative to HTHH by a distance depending on the emission height. For an emission height of 17 km (lower umbrella) and 32 km (upper umbrella) the shift is ~20 and ~38 km, respectively, or $\mathcal{O}(10 \, \text{pixels})$.

The center of the ellipse fitted to one of the concentric rings in Figure 15a is located ~192 km west of an assumed emission source at ~22 km (peak of C12 weighting function). Note that the uncertainty of ellipse fitting can easily be on the order of 10 km, because the concentric rings are not perfect circles (or ellipses in the satellite perspective) due to anisotropic propagation and they might only be partially observed. Here, we focused on fitting the northern and western part of the rings, which are the clearest in the images.

The semi major axis of the fitted ellipse is ~461 km, which corresponds to a travel time of ~59 min from emission assuming a propagation velocity of 130 m s^{-1}. This, in turn, corresponds to a mean westward advection speed of the ellipse center of ~54 m s^{-1}. By fitting several concentric rings, we estimate a typical westward advection speed of 50–60 m s^{-1}, which is within the range of the stereo plume motion retrievals by Carr et al. (2022). The largest ring in Figure 15a indicates a travel time of ~75 min; therefore, these GWs were likely triggered by a later explosion which started between 05:44–05:51 UTC according to surface pressure records (Purkis et al., 2023; Wright et al., 2022).
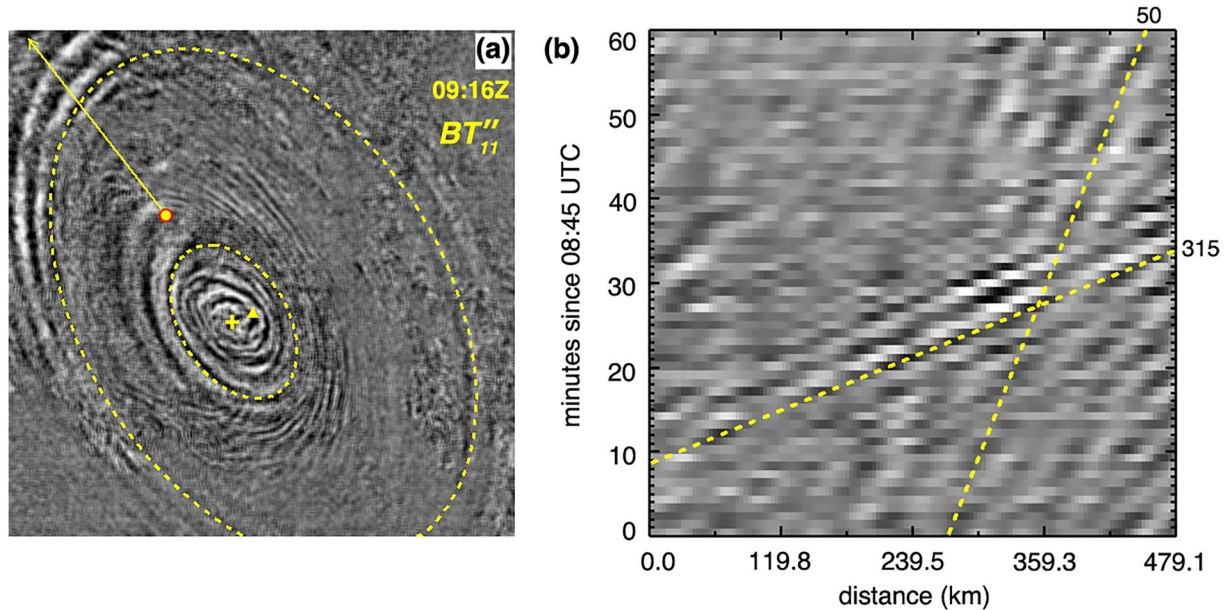
Figure 16. Lamb and gravity waves in G17_M1 (HTHH) triggered by the last major explosion on 15 January 2022: (a) BT''_{11} at 09:16 UTC and (b) time–distance plot for the period 08:45–09:45 UTC along the yellow arrow in panel (a). The interval used for calculating the time derivatives is $\Delta t = 1$ min and the stack plot is based on FFT-filtered images. The larger ellipse fitted to a Lamb wave ring is a circle with a radius of 585 km centered on HTHH (triangle), while the smaller ellipse fitted to a GW ring is a circle of 175 km radius with a shifted center (plus sign).

4.2.3. Lamb Waves From the Last Major Explosion

Our final example using the GOES-17 M1 HTHH imagery demonstrates the detection of Lamb waves triggered by the last major eruption ∼4.0–4.5 hr after the primary climactic event. The 10.3-μm brightness temperatures show several cold bubbles rising to 30+ km altitude between 8 and 9 UTC (Movie S11 in Supporting Information S1; Carr et al., 2022), with the two most prominent ones occurring at 08:41 UTC (∼168 K) and 08:46 UTC (∼172 K). Stereo motion retrievals by Carr et al. (2022) reveal strong plume-top divergence as these bubbles reach the upper umbrella and spread out. The global infrasound and seismo-acoustic network detected an explosive event at 08:31 UTC (Matoza et al., 2022), while the Tonga surface pressure data indicate the last major signal at 08:46 UTC (Wright et al., 2022).

This series of explosions generated Lamb waves as well as GWs, as depicted in Figure 16 (see also Movie S14 in Supporting Information S1). The animations show a fast-moving packet of waves in the top left (northwestern) quadrant of the domain between ∼08:55–09:30 UTC. The stack plot in Figure 16b yields a propagation speed of ∼315 m s^{-1} and horizontal wavelength of ∼60–70 km, similar to the Lamb waves generated by the primary explosion. Unlike the primary Lamb waves, however these weaker secondary Lamb waves could not be detected in the far-field domains. Note that the concentric rings in Figure 16a can be well fitted with circles centered on HTHH. This indicates negligible parallax in the projected location of the emission center, which is further proof of surface-triggered Lamb waves that coherently move through the troposphere guided by weak near-surface winds.

In contrast, the smaller concentric rings visible in the upper umbrella can only be fitted with circles whose center is shifted west-southwest relative to HTHH due mostly to parallax and to a lesser degree wind. This indicates gravity waves emitted at 30+ km altitude. A time–distance analysis (not shown) reveals that the spectral characteristics of these GWs (wavelength of ∼40 km and speed of ∼135 m s^{-1}) are similar to those of the earlier-emitted GWs plotted in Figure 15. Figure 16b also hints at the presence of slower GWs propagating at a speed of ∼40–50 m s^{-1}. These small-scale GWs detected in the plume are consistent with the dense concentric wave patterns observed by AIRS at a somewhat larger distance from the volcano (Adam, 2022).

5. Discussion and Summary

We analyzed GOES-R high-cadence mesoscale imagery to estimate the spectral properties of Lamb and gravity waves emitted by the 15 January 2022 HTHH eruption. In a $\sim 1{,}000 \times 1{,}000$ km^2 domain, the 1-min mesoscale brightness temperatures provide an order of magnitude better temporal sampling than the 10-min or 15-min full-disk data used in previous studies. The absolute temperature perturbations produced by the eruption are generally difficult to extract, because they are superimposed on a large dynamic range and highly variable background. Instead, we used the common visualization method of differencing *BT* image sequences, which amounts to taking the time derivatives of the waveform. The appearance of wave patterns in such difference imagery is controlled by two opposing factors. Waveform derivatives represent a high-pass filter, which eliminates the long period variation. Contrarily, reducing the observation frequency, as in full-disk data, leads to the temporal aliasing of short-period fluctuations to longer periods and wavelengths.

The surface pressure signature of the HTHH Lamb waves contains multiple pulses of varying magnitude, but its broad envelope can be approximated by an *N*-wave or positive triangular pulse of 20–50 min duration and 400–900 km width, depending on location. We showed that imposing temperature anomalies that trace the measured surface pressure anomalies explains the salient features of the BT'' second derivative patterns seen in the high-cadence mesoscale imagery. These patterns visualize the short-period variations and individual shocks within the wave packet rather than the broad envelope. However, the full temperature anomaly waveform can be reconstructed reasonably well from the observed mesoscale BT''. The reconstructed temperature anomalies highly correlate with the measured pressure anomalies.

In contrast, the temporally aliased full-disk data only captures the primary Lamb pulse, which can be approximated by an *N*-wave with a duration of 30–40 min. In the low-cadence full-disk BT'' images, the primary Lamb pulse appears as a bright–dark–bright triplet of ~ 200 km wide bands (the distance an acoustic packet travels in 10 min).

The mesoscale imagery indicates that the primary Lamb wave is trailed by long-continuing waves of ~ 40–80 km wavelength. With the estimated horizontal phase velocity of $\sim 315 \pm 15$ m s^{-1}, the trailing waves have typical periods of 2.1–4.2 min and frequencies of 4–8 mHz. The mesoscale data also suggest dispersion, because wavelength tends to systematically decrease with time as the wave train traverses the domains.

These transient volcanic Lamb frequencies are well within the 0.2–10 mHz frequency range of turbulence-induced background Lamb waves, which are generally present in the atmosphere (Nishida et al., 2014). The short acoustic periods observed in our data are also in agreement with early findings on atmospheric nuclear explosions and other major volcanic eruptions. We note that most of the early works analyzed data from microbarovariographs, which are high-pass instruments. They measure the rate of change of pressure (the first time derivative) rather than the absolute pressure; thus, they are readily comparable with our observations of *BT* waveform derivatives.

The oscillatory part of microbarovariograms recorded after nuclear tests contains dominant wavelengths less than 100 km and periods of 1–10 min (Donn et al., 1963; Donn & Ewing, 1962; Garrett, 1969; Pierce & Posey, 1971; Posey & Pierce, 1971). Waves from nuclear explosions are also dispersive, such that in the far field the initial impulse becomes resolved into a train of waves of decreasing period. Concerning volcanic eruptions, Bolt and Tanimoto (1981) and Mikumo and Bolt (1985) found atmospheric pressure waves from the 1980 Mount St. Helens eruption with dominant periods of 5–8 min, while Kanamori et al. (1994) report atmospheric oscillations with periods of 3–5 min for the 1883 Krakatoa, the 1982 El Chicón, and the 1991 Pinatubo eruptions as well.

Acoustic waves with a period of ~ 5 min are thus often generated by energetic atmospheric blasts. A recent analysis of HTHH air and seafloor pressure spectrograms by Tonegawa and Fukao (2023) also identified long-continuing waves at frequencies near 3.6 mHz (period of ~ 4.6 min), which bear a close resemblance to the trailing waves observed in our satellite imagery. They argue that these waves represent the resonant coupling of the main Lamb wave and thermospheric gravity waves that propagate horizontally at the sound speed. The long-period primary Lamb wave can be adequately generated by a sea level or mid-tropospheric pressure source (Amores et al., 2022; Watanabe et al., 2022). The excitation of the primary Lamb wave together with the shorter period Lamb waves, thermospheric waves, and the resonant waves, however, requires a more energetic pressure source located in the mesosphere.

Besides the climactic explosion at ~04:29 UTC, Lamb waves were generated by the last major explosion at ~08:40–08:45 UTC too. These weaker waves, however, could only be observed in the near-field but not in the far-field domains. The mesoscale data also proved useful to detect wind effects such as mean flow advection in the propagation of gravity waves and captured gravity waves propagating near their theoretical maximum speed (~130 m s^{-1} for a wavelength of ~42 km).

In conclusion, the GOES-R mesoscale observations represent a rich data source for further work. More sophisticated analysis techniques (e.g., wavelet transform) could be used to extract additional spectral information, confirm Lamb wave dispersion, and exploit IR channel differences in order to characterize the 3D nature and vertical propagation of waves. The data could also be used to constrain the HTHH eruption source parameters and validate the detailed numerical modeling of global wave propagation.

Data Availability Statement

GOES-16 and GOES-17 datasets are publicly accessible through Amazon Web Services (AWS, 2023). ERA5 data are available from Hersbach et al. (2017). The Pago Pago, American Samoa surface pressure data (sensor index 85435) are freely available for non-commercial use after registration at PurpleAir (2023). The Coconut Point, American Samoa surface pressure data are from the personal weather station of Joe LaPlante (joseph.laplante@noaa.gov) and are included in the Supporting Information submitted with this paper. The publicly available ASOS Page 2 station data are provided by ASOS (2023).

References

Adam, D. (2022). Tonga volcano created puzzling atmospheric ripples. *Nature*, *602*, 497. https://doi.org/10.1038/d41586-022-00127-1

Amores, A., Monserrat, S., Marcos, M., Argüeso, D., Villalonga, J., Jordà, G., & Gomis, D. (2022). Numerical simulation of atmospheric Lamb waves generated by the 2022 Hunga-Tonga volcanic eruption. *Geophysical Research Letters*, *49*(6), e2022GL098240. https://doi.org/10.1029/2022GL098240

ASOS. (2023). National centers for environmental information (NCEI). Dataset. Retrieved from https://www.ncei.noaa.gov/data/automated-surface-observing-system-one-minute-pg2/

Averiyanov, M., Ollivier, S., Khokhlova, V., & Blanc-Benon, P. (2011). Random focusing of nonlinear acoustic *N*-waves in fully developed turbulence: Laboratory scale experiment. *Journal of the Acoustical Society of America*, *130*(6), 3595–3607. https://doi.org/10.1121/1.3652869

AWS. (2023). Amazon Web Services (AWS). Dataset. Retrieved from https://registry.opendata.aws/noaa-goes/

Bolt, B. A., & Tanimoto, T. (1981). Atmospheric oscillations after the May 18, 1980 eruption of Mount St. Helens. *Eos Transactions American Geophysical Union*, *62*(23), 529–530. https://doi.org/10.1029/EO062i023p00529

Bór, J., Bozóki, T., Sátori, G., Williams, E., Behnke, S. A., Rycroft, M. J., et al. (2023). Responses of the AC/DC global electric circuit to volcanic electrical activity in the Hunga Tonga-Hunga Ha'apai eruption on 15 January 2022. *Journal of Geophysical Research: Atmospheres*, *128*(8), e2022JD038238. https://doi.org/10.1029/2022JD038238

Bretherton, F. P. (1969). Lamb waves in a nearly isothermal atmosphere. *Quarterly Journal of the Royal Meteorological Society*, *95*(406), 754–757. https://doi.org/10.1002/qj.49709540608

Carr, J. L., Horváth, Á., Wu, D. L., & Friberg, M. D. (2022). Stereo plume height and motion retrievals for the record-setting Hunga Tonga-Hunga Ha'apai eruption of 15 January 2022. *Geophysical Research Letters*, *49*(9), e2022GL098131. https://doi.org/10.1029/2022GL098131

Donn, W. L., & Ewing, M. (1962). Atmospheric waves from nuclear explosions—Part II: The soviet test of 30 October 1961. *Journal of the Atmospheric Sciences*, *19*(3), 264–273. https://doi.org/10.1175/1520-0469(1962)019<0264:awfnei>2.0.co;2;2

Donn, W. L., Pfeffer, R. L., & Ewing, M. (1963). Propagation of air waves from nuclear explosions. *Science*, *139*(3552), 307–317. https://doi.org/10.1126/science.139.3552.307

Francis, S. H. (1973). Acoustic-gravity modes and large-scale traveling ionospheric disturbances of a realistic, dissipative atmosphere. *Journal of Geophysical Research*, *78*(13), 2278–2301. https://doi.org/10.1029/JA078i013p02278

Garrett, C. J. R. (1969). Atmospheric edge waves. *Quarterly Journal of the Royal Meteorological Society*, *95*(406), 731–753. https://doi.org/10.1002/qj.49709540607

GOES R. (2019). GOES R series product definition and user's guide (PUG), 416-R-PUG-L1B-0347 Vol. 3 Revision 2.2. Retrieved from https://www.goes-r.gov/users/docs/PUG-L1b-vol3.pdf

Harding, B. J., Wu, Y.-J. J., Alken, P., Yamazaki, Y., Triplett, C. C., Immel, T. J., et al. (2022). Impacts of the January 2022 Tonga volcanic eruption on the ionospheric dynamo: ICON-MIGHTI and swarm observations of extreme neutral winds and currents. *Geophysical Research Letters*, *49*(9), e2022GL098577. https://doi.org/10.1029/2022GL098577

Heinrich, P., Gailler, A., Dupont, A., Rey, V., Hébert, H., & Listowski, C. (2023). Observations and simulations of the meteotsunami generated by the Tonga eruption on 15 January 2022 in the Mediterranean Sea. *Geophysical Journal International*, *234*(2), 903–914. https://doi.org/10.1093/gji/ggad092

Heki, K. (2022). Ionospheric signatures of repeated passages of atmospheric waves by the 2022 Jan. 15 Hunga Tonga-Hunga Ha'apai eruption detected by QZSS-TEC observations in Japan. *Earth Planets and Space*, *74*(1), 112. https://doi.org/10.1186/s40623-022-01674-7

Hersbach, H., Bell, B., Berrisford, P., Hirahara, S., Horányi, A., Muñoz-Sabater, J., et al. (2017). Complete ERA5 from 1940: Fifth generation of ECMWF atmospheric reanalyses of the global climate [dataset]. Copernicus Climate Change Service (C3S) Climate Data Store (CDS). https://doi.org/10.24381/cds.143582cf

Johnson, J. B., Boyer, T., Watson, L. M., & Anderson, J. F. (2023). Volcano opto-acoustics: Mapping the infrasound wavefield at Yasur Volcano (Vanuatu). *Geophysical Research Letters*, *50*(8), e2022GL102029. https://doi.org/10.1029/2022GL102029

Kanamori, H., Mori, J., & Harkrider, D. G. (1994). Excitation of atmospheric oscillations by volcanic eruptions. *Journal of Geophysical Research*, *99*(B11), 21947–21961. https://doi.org/10.1029/94JB01475

Khaykin, S., Podglajen, A., Ploeger, F., Grooß, J.-U., Tence, F., Bekki, S., et al. (2022). Global perturbation of stratospheric water and aerosol burden by Hunga eruption. *Communications Earth & Environment*, *3*(1), 316. https://doi.org/10.1038/s43247-022-00652-x

Kubota, T., Saito, T., & Nishida, K. (2022). Global fast-traveling tsunamis driven by atmospheric Lamb waves on the 2022 Tonga eruption. *Science*, *377*(6601), 91–94. https://doi.org/10.1126/science.abo4364

Matoza, R. S., Fee, D., Assink, J. D., Iezzi, A. M., Green, D. N., Kim, K., et al. (2022). Atmospheric waves and global seismoacoustic observations of the January 2022 Hunga eruption, Tonga. *Science*, *377*(6601), 95–100. https://doi.org/10.1126/science.abo7063

McCorkel, J., Van Naarden, J., Lindsey, D., Efremova, B., Coakley, M., Black, M., & Krimchansky, A. (2019). GOES-17 advanced baseline imager performance recovery summary. In *Proceedings of IGARSS 2019 – IEEE International Geoscience and Remote Sensing Symposium*. https://doi.org/10.1109/igarss40859.2019.9044466

Mikumo, T., & Bolt, B. A. (1985). Excitation mechanism of atmospheric pressure waves from the 1980 Mount St Helens eruption. *Geophysical Journal International*, *81*(2), 445–461. https://doi.org/10.1111/j.1365-246X.1985.tb06412.x

Millán, L., Santee, M. L., Lambert, A., Livesey, N. J., Werner, F., Schwartz, M. J., et al. (2022). The Hunga Tonga-Hunga Ha'apai hydration of the stratosphere. *Geophysical Research Letters*, *49*(13), e2022GL099381. https://doi.org/10.1029/2022GL099381

Nishida, K., Kobayashi, N., & Fukao, Y. (2014). Background Lamb waves in the Earth's atmosphere. *Geophysical Journal International*, *196*(1), 312–316. https://doi.org/10.1093/gji/ggt413

Otsuka, S. (2022). Visualizing Lamb waves from a volcanic eruption using meteorological satellite Himawari-8. *Geophysical Research Letters*, *49*(8), e2022GL098324. https://doi.org/10.1029/2022GL098324

Pierce, A. D., & Posey, J. W. (1971). Theory of the excitation and propagation of Lamb's atmospheric edge mode from nuclear explosions. *Geophysical Journal International*, *26*(1–4), 341–368. https://doi.org/10.1111/j.1365-246X.1971.tb03406.x

Posey, J. W., & Pierce, A. D. (1971). Estimation of nuclear explosion energies from microbarograph records. *Nature*, *232*(5308), 253. https://doi.org/10.1038/232253a0

Proud, S. R., Prata, A. T., & Schmauss, S. (2022). The January 2022 eruption of Hunga Tonga-Hunga Ha'apai volcano reached the mesosphere. *Science*, *378*(6619), 554–557. https://doi.org/10.1126/science.abo4076

Purkis, S. J., Ward, S. N., Fitzpatrick, N. M., Garvin, J. B., Slayback, D., Cronin, S. J., et al. (2023). The 2022 Hunga-Tonga megatsunami: Near-field simulation of a once-in-a-century event. *Science Advances*, *9*(15), eadf5493. https://doi.org/10.1126/sciadv.adf5493

PurpleAir (2023). PurpleAir, Inc. Dataset. Retrieved from https://www2.purpleair.com/

Randel, W. J., Johnston, B. R., Braun, J. J., Sokolovskiy, S., Vömel, H., Podglajen, A., & Legras, B. (2023). Stratospheric water vapor from the Hunga Tonga–Hunga Ha'apai volcanic eruption deduced from COSMIC-2 radio occultation. *Remote Sensing*, *15*(8), 2167. https://doi.org/10.3390/rs15082167

Schmit, T. J., Griffith, P., Gunshor, M. M., Daniels, J. M., Goodman, S. J., & Lebair, W. J. (2017). A closer look at the ABI on the GOES-R Series. *Bulletin of the American Meteorological Society*, *98*(4), 681–698. https://doi.org/10.1175/BAMS-D-15-00230.1

Sepúlveda, I., Carvajal, M., & Agnew, D. C. (2023). Global winds shape planetary-scale Lamb waves. *Geophysical Research Letters*, *50*(19), e2023GL106097. https://doi.org/10.1029/2023GL106097

Stout, T. A. (2018). Simulation of N-wave and shaped supersonic signature turbulent variations, (Doctoral dissertation). The Pennsylvania state University. Retrieved from Electronic Theses and Dissertations for Graduate School (ETDA). Retrieved from https://etda.libraries.psu.edu/catalog/15959tqs5346

Suzuki, T., Nakano, M., Watanabe, S., Tatebe, H., & Takano, Y. (2023). Mechanism of a meteorological tsunami reaching the Japanese coast caused by Lamb and Pekeris waves generated by the 2022 Tonga eruption. *Ocean Modelling*, *181*, 102153. https://doi.org/10.1016/j.ocemod.2022.102153

Tonegawa, T., & Fukao, Y. (2023). Mesospheric pressure source from the 2022 Hunga, Tonga eruption excites 3.6-mHz air-sea coupled waves. *Science Advances*, *9*(26), eadg8036. https://doi.org/10.1126/sciadv.adg8036

Vadas, S. L. (2013). Compressible *f*-plane solutions to body forces, heatings, and coolings, and application to the primary and secondary gravity waves generated by a deep convective plume. *Journal of Geophysical Research: Space Physics*, *118*(5), 2377–2397. https://doi.org/10.1002/jgra.50163

Vadas, S. L., Becker, E., Figueiredo, C., Bossert, K., Harding, B. J., & Gasque, L. C. (2023). Primary and secondary gravity waves and large-scale wind changes generated by the Tonga volcanic eruption on 15 January 2022: Modeling and comparison with ICON-MIGHTI winds. *Journal of Geophysical Research: Space Physics*, *128*(2), e2022JA031138. https://doi.org/10.1029/2022JA031138

Vadas, S. L., Figueiredo, C., Becker, E., Huba, J. D., Themens, D. R., Hindley, N. P., et al. (2023b). Traveling ionospheric disturbances induced by the secondary gravity waves from the Tonga eruption on 15 January 2022: Modeling with MESORAC/HIAMCM/Sami3 and comparison with GPS/TEC and ionosonde data. *Journal of Geophysical Research: Space Physics*, *128*(6), e2023JA031408. https://doi.org/10.1029/2023JA031408

Vadas, S. L., Yue, J., She, C.-Y., Stamus, P. A., & Liu, A. Z. (2009). A model study of the effects of winds on concentric rings of gravity waves from a convective plume near Fort Collins on 11 May 2004. *Journal of Geophysical Research*, *114*(D6), D06103. https://doi.org/10.1029/2008JD010753

Van Eaton, A. R., Lapierre, J., Behnke, S. A., Vagasky, C., Schultz, C. J., Pavolonis, M., et al. (2023). Lightning rings and gravity waves: Insights into the giant eruption plume from Tonga's Hunga Volcano on 15 January 2022. *Geophysical Research Letters*, *50*(12), e2022GL102341. https://doi.org/10.1029/2022GL102341

Vergoz, J., Hupe, P., Listowski, C., Le Pichon, A., Garcés, M. A., Marchetti, E., et al. (2022). IMS observations of infrasound and acoustic-gravity waves produced by the January 2022 volcanic eruption of Hunga, Tonga: A global analysis. *Earth and Planetary Science Letters*, *591*, 117639. https://doi.org/10.1016/j.epsl.2022.117639

Watada, S., Imanishi, Y., & Tanaka, K. (2023). Detection of air temperature and wind changes synchronized with the Lamb wave from the 2022 Tonga volcanic eruption. *Geophysical Research Letters*, *50*(2), e2022GL100884. https://doi.org/10.1029/2022GL100884

Watanabe, S., Hamilton, K., Sakazaki, T., & Nakano, M. (2022). First detection of the Pekeris internal global atmospheric resonance: Evidence from the 2022 Tonga eruption and from global reanalysis data. *Journal of the Atmospheric Sciences*, *79*(11), 3027–3043. https://doi.org/10.1175/JAS-D-22-0078.1

Winn, S., Sarmiento, A., Alferez, N., & Touber, E. (2023). Two-way coupled long-wave isentropic ocean-atmosphere dynamics. *Journal of Fluid Mechanics*, *959*, A22. https://doi.org/10.1017/jfm.2023.131

Wright, C. J., Hindley, N. P., Alexander, M. J., Barlow, M., Hoffmann, L., Mitchell, C. N., et al. (2022). Surface-to-space atmospheric waves from Hunga Tonga–Hunga Ha'apai eruption. *Nature*, *609*(7928), 741–746. https://doi.org/10.1038/s41586-022-05012-5

Yamada, M., Ho, T.-C., Mori, J., Nishikawa, Y., & Yamamoto, M.-Y. (2022). Tsunami triggered by the Lamb wave from the 2022 Tonga volcanic eruption and transition in the offshore Japan region. *Geophysical Research Letters*, *49*(15), e2022GL098752. https://doi.org/10.1029/2022GL098752

Yuldashev, P. V., Ollivier, S., Karzova, M. M., Khokhlova, V. A., & Blanc-Benon, P. (2017). Statistics of peak overpressure and shock steepness for linear and nonlinear *N*-wave propagation in a kinematic turbulence. *Journal of the Acoustical Society of America*, *142*(6), 3402–3415. https://doi.org/10.1121/1.5015991